A FIELD ION MICROSCOPE STUDY OF INTERFACES

A FIELD ION MICROSCOPE STUDY OF INTERFACES

By

RAMESH RAJAGOPAL, B.TECH.

A Thesis
Submitted to the School of Graduate Studies
in Partial Fulfilment of the Requirements
for the Degree
Master of Engineering
McMaster University
(July) 1972

MASTER OF ENGINEERING (1972)
(Metallurgy and Materials Science)

McMASTER UNIVERSITY
Hamilton, Ontario.

TITLE: A Field Ion Microscope Study of Interfaces

AUTHOR: Ramesh Rajagopal, B.Tech. (Indian Institute of Technology, Bombay.)

SUPERVISORS: Dr. G. R. Purdy and Dr. P. T. Dawson

NUMBER OF PAGES: iv, 103.

SCOPE AND CONTENTS:

This investigation is concerned with the observation of interfaces between f.c.c. and b.c.c. crystals in the field ion microscope. A high vacuum field ion microscope was designed and constructed to operate under liquid nitrogen cooling and helium gas imaging, with facilities for vapour deposition. Platinum and iridium were deposited on tungsten field ion emitters by shadow vapour deposition.

The nature and contrast of deposits obtained under various experimental conditions are examined. The atomic matching observed at interfaces is discussed within the limitations of the existing interfacial contrast theory.

ACKNOWLEDGEMENT

I wish to express my sincere thanks to Dr. G. R. Purdy and Dr. P. T. Dawson for their encouragement and guidance through all the stages of this project.

I am indebted to Dr. B. Ralph of Cambridge University, England, for his expert comments on the design of the field ion microscope. I am grateful to several workers in this field from the Pennsylvania State University, University Park, and Columbia University, New York for initiating me into field ion microscopy.

I greatly appreciate the personal interest Dr. G. R. Piercy has shown during my illness.

I wish to thank my fellow graduate students, especially Mr. D. E. Stephens for several fruitful discussions and the technical staff for help with laboratory work.

TABLE OF CONTENTS

PAGE

INTRODUCTION 1

CHAPTER 1 FIELD ION MICROSCOPY 2

- 1.1 Introduction 2
- 1.2 Principles of field ion microscopy 4
- 1.3 Field ionization 7
  - 1.3.1 Mechanism of field ionization 7
  - 1.3.2 Field ion current 13
    - (a) Ion current 13
    - (b) Gas supply function 14
    - (c) Current voltage characteristics 15
  - 1.3.3 Magnification and resolution 18
    - (a) Magnification 18
    - (b) Resolution 19
- 1.4 Field evaporation 20
  - 1.4.1 Image force theory 21
  - 1.4.2 Field evaporation models 23
  - 1.4.3 Polarization effect 26
  - 1.4.4 Field evaporation end form 27
  - 1.4.5 Effect of image gases 28
- 1.5 Image interpretation 29
  - 1.5.1 Indexing and radius of curvature 29

1.5.2 Regional image brightness and zone decoration 30
1.5.3 Distribution of surface charge 31
1.5.4 Artefacts 31
1.5.5 Observation of defects 32
1.5.6 Determination of grain boundary parameters 32
(a) Low angle grain boundaries 33
(b) High angle grain boundaries 33
1.5.7 Contrast from alloys 35
CHAPTER 2 THIN FILMS 38
2.1 Introduction 38
2.2 Preparation of thin films 38
2.3 Nucleation and growth of thin films 39
2.4 Alloying during deposition 40
CHAPTER 3 INTERPHASE BOUNDARIES 42
3.1 Introduction 42
3.2 Incoherent or disordered boundaries 43
3.3 Partially coherent or dislocation boundaries 44
CHAPTER 4 EXPERIMENTAL 47
4.1 Design of an all-glass high vacuum FIM 47
4.1.1 Vacuum system 47
4.1.2 Microscope chamber, specimen holder and screen 49
4.1.3 Image gas 51

4.1.4 Specimen coolant 51
4.2 Accessories 51
4.2.1 High voltage supply 51
4.2.2 Pulse field evaporation circuit 51
4.2.3 Tip heating circuit 54
4.2.4 High voltage isolation switch 54
4.2.5 Metal vapour source 54
4.2.6 Power supply for the vapour source 54
4.3 Photography 54
4.4 Tip preparation 56
4.5 Experimental run 56
CHAPTER 5 RESULTS AND DISCUSSION 60
5.1 Analysis of a high angle grain boundary 60
5.2 Choice of the systems for vapour deposition experiments 64
5.3 Deposition of platinum on tungsten 66
5.4 Deposition of iridium on tungsten I 70
5.5 Deposition of iridium on tungsten II 76
5.5.1 Deposit annealed at 1200°C for 3 hours 76
5.5.2 Deposit annealed at 800°C for 1 1/4 hours 81
5.5.3 Deposit annealed at 900°C for 2 hours 84
CHAPTER 6 CONCLUSIONS 93
SUGGESTION FOR FUTURE WORK 95
REFERENCES 97

INTRODUCTION

Interphase boundaries in various alloy systems have been the subject of intense research in recent years. Current theories of precipitate morphology are based on the concept of phase boundary mobility. The mobility of the interphase boundary depends on the atomic structure of the interface. Detailed study of these interfaces has been limited in the past by the limited resolution of the experimental techniques. Development of the field ion microscope has provided researchers the unique opportunity of observing the structure of interfaces in atomic detail.

A lot of effort has been concentrated on the study of grain boundary structure using the field ion microscope, whereas, not much work has been done on two-phase interfaces.

A field ion microscope was designed to conduct in-situ vapour deposition experiments. Platinum and iridium (f.c.c.) were shadow vapour deposited on tungsten (b.c.c.) substratesto artificially produce interfaces resembling two-phase boundaries. An epitaxial relation (such as Kurdjumon-Sachs orientation relation) between the deposit and the substrate would present a situation similar to Widmanstätten precipitates in b.c.c./f.c.c. systems. This would enable the observation of interfaces resembling the broad faces of Widmanstätten plates (dislocation interphase boundaries) as well as interfaces resembling the tip of Widmanstätten plates (disordered interphase boundaries).

CHAPTER 1

FIELD ION MICROSCOPY

1.1 Introduction

Field ion microscopy is the only means known today for directly viewing the structure of solid surfaces in atomic detail (Fig.1.1). The field ion microscope offers a magnification of up to several million diameters and a resolution often between 2 to 3 Å. This is not easily achieved by other complementary techniques such as routine transmission electron microscopy. Earlier, field ion microscopy was restricted to the observation of refractory metals and their alloys. Now, the observation of less refractory metals and alloys in the FIM is a fairly standard procedure, although the quality of the image obtained is not as good as that obtained from the more refractory metals.

The applications of the FIM can be classified into two categories: study of surface phenomena, such as surface diffusion and adsorption; and the study of bulk phenomena. Field ion microscopy has been widely used in the study of extensive features, such as the structure of grain boundaries, the clusturing of solute atoms, interstitials or vacancies and the morphology of precipitates. The investigation of features on the atomic scale, e.g. the atom position at an interface or a dislocation core, is potentially more rewarding, but, inevitably more difficult.

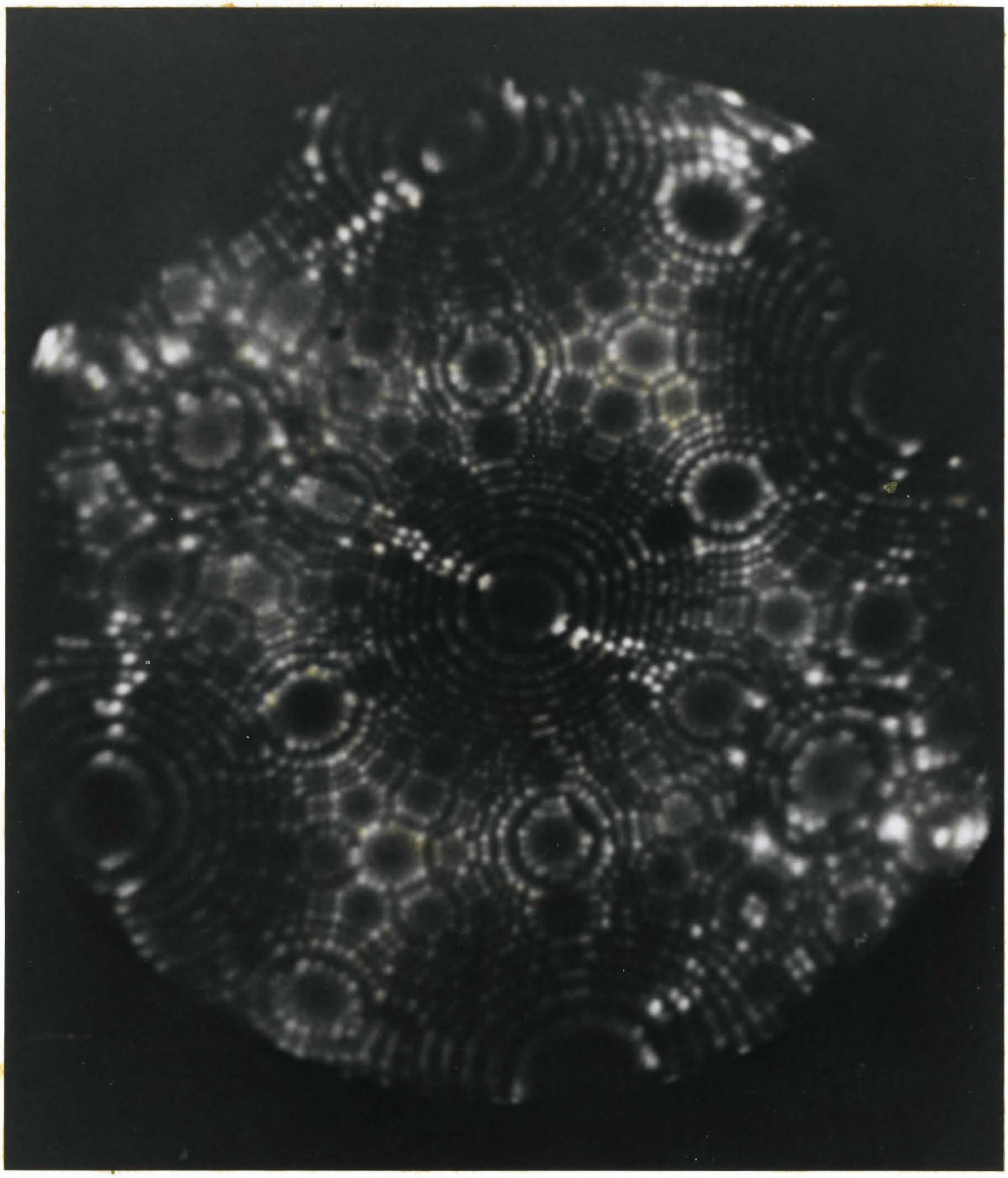

Figure 1.1 A field ion micrograph of tungsten.

This chapter deals with the physical principles of the microscope and the interpretation of field ion micrographs. Some reviews concentrating on the physical processes are those of Müller(1), Gomer (2), Brandon(3), Southon(4) and Müller and Tsong(5).

1.2 Principles of field ion microscopy

The field ion microscope (FIM)(1) was developed from its forerunner, the field electron emission microscope (FEM)(6). The simplest type of FEM consists of a sharp needle of a metal (1,000-10,000 Å radius) acting as the cathode, with a fluorescent screen opposite to this tip as the anode, both being mounted in a highly evacuated (less than 10^{-9} torr) glass tube. Electrons from different crystallographic regions of the hemispherical cap tunnel out when the applied field is of the order of 0.3-0.5 volts/Å. The experiments are done at cryogenic temperatures and the magnification obtained could be up to one million, whereas the resolution limit is about 25 Å.

The essential features of the FIM (see figure 1.2) are the same except that the specimen tip radius is still smaller i.e. 100-1,000 Å and is kept at a positive potential with the screen grounded. The vacuum conditions are moderate ($\simeq 10^{-6}$ torr). The tube is filled with the imaging gas to $\simeq 10^{-3}$ torr for maximum image brightness without loss of resolution by ion-gas atom scattering. The fields required to ionize the image gases vary from 2 to 6 V/Å - an order of magnitude greater than the negative fields required for the field emission of electrons. The image gas ions are produced in the immediate proximity of the specimen surface by a process known as field

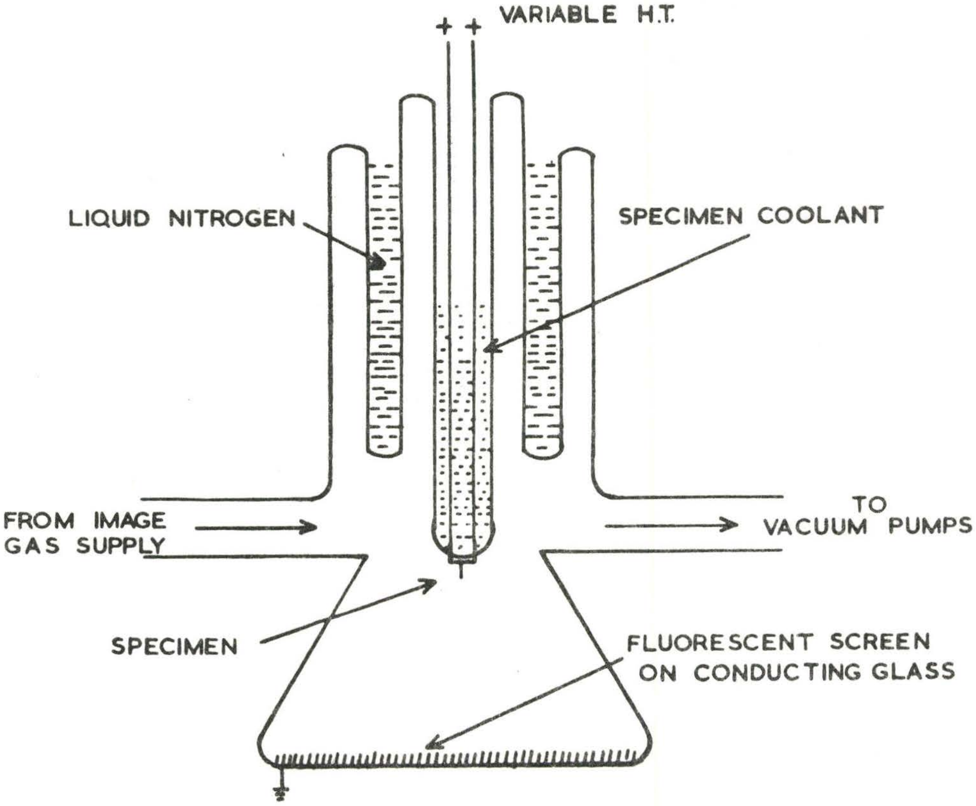

Figure 1.2 The basic design of a field ion microscope.

ionization(1). The image information is carried from the tip surface to the screen by radially projected positive ions. The magnification is up to a few million diameters and the resolution is between 2-3 Å.

Two essential features of the FIM are the provision for cooling the tip by heat conduction through its leads from a 'cold finger' filled with a cryogenic liquid and a flat phosphorescent screen which is required for photographing the weak images using a high aperture objective having a low depth of focus.

The surface of a freshly etched field ion specimen is uneven and atomically very rough. As the field on the specimen is increased, the local field at the protuberant sites gets exceedingly high, so that the metal atoms evaporate even at cryogenic temperatures. This process known as 'field evaporation'(1) is continued as long as asperities remain on the surface, resulting eventually in the field evaporation end form which is atomically smooth and crystallographically as perfect as the bulk specimen. Once the end form is established, field evaporation can be continued at a controlled rate to explore the internal structure by bringing it to the surface.

By combining a field ion microscope having a small probe hole in the screen with a time-of-flight mass spectrometer, the atomic species of an image dot can be identified by pulse field evaporation of the chosen atom through the probe hole. This device termed as the atom-probe field ion microscope(7) is the only device capable of identifying a selected single atom on a metal surface. It is hoped that the general application of this ultimate system of microanalysis will solve many of the still open questions in field ion microscopy and more generally in materials research.

1.3 Field Ionization

1.3.1 The mechanism of field ionization

Field ionization is a process in which the electron in an atom tunnels through its potential barrier which is modified by the presence of an electric field.

The potential energy of an electron in a gas atom is shown in figure 1.3(a). An energy equivalent to the ionization potential I must be supplied to ionize the atom. In the presence of an electric field, the potential barrier of the electron would be as shown in figure 1.3(b). When the atom is in the proximity of a metal surface, the potential barrier is further modified due to image forces(8) (see figure 1.3(c)). The potential energy V(x) can be approximately expressed as(9)

$$V(x) = -\frac{e^2}{|x_i - x|} + eFx - \frac{e^2}{4x} + \frac{e^2}{x_i + x} \qquad (1.1)$$

where F is the electric field

x is the distance of the electron from the metal surface

x_i is the distance of the ion from the metal surface.

The first term gives the potential energy due to the positive ion; The second gives the potential energy of the electron due to the applied field; the third and the fourth give the potential energies due to the electron's positive image and the negative image of the ion behind the conductor surface.

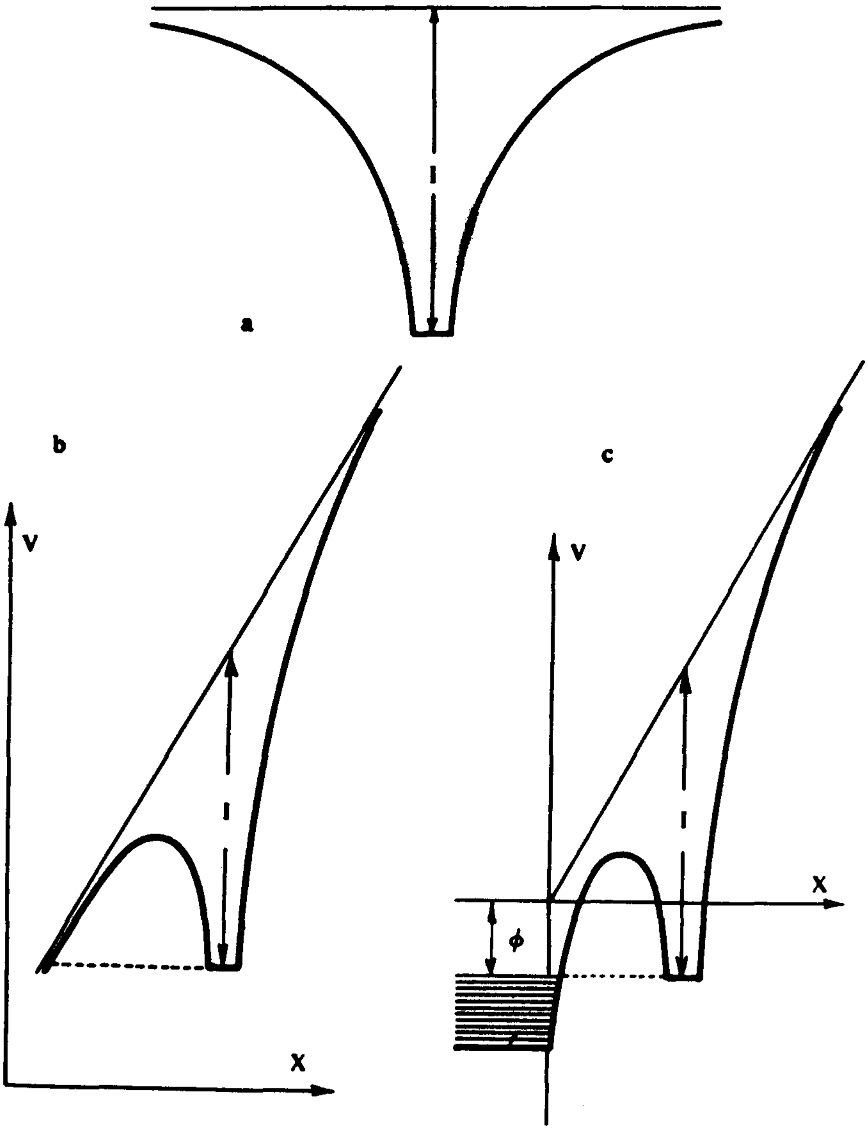

Figure 1.3 (a) Potential energy of an electron of an atom.

(b) Potential energy of an electron of an atom in an electric field.

(c) Potential energy of an electron of an atom near a metal surface$^{(5)}$.

The closest distance x_c at which the atom can still be ionized is determined by the condition that the ground state of the atom is just above the Fermi level in the metal. This critical distance x_c is defined by the equation

$$Fex_c = I - \phi - \frac{e^2}{4x_c} \tag{1.2}$$

where ϕ is the work function of the metal.

Neglecting the image potential term, we obtain an expression for x_c as

$$x_c = \frac{I-\phi}{Fe} \tag{1.3}$$

x_c is found to lie in the range of 4-8 Å for most gases likely to be used in field ion microscopy. At distances less than x_c, the ground state of the electron in the atom falls below the fermi level in the metal and the metal will not accept any electrons because all the levels below the Fermi energy are filled (Pauli exclusion principle).

The probability of the electron in the gas atom tunneling through the potential barrier is appreciable when the electric field is high enough to reduce the width of the barrier to a value comparable to the Debroglie wavelength of the electron in the gas atom. The penetration probability of a one dimensional barrier using the WKB approximation$^{(10)}$ is given by

$$D(E,V) = \exp\{-(\frac{8m}{\hbar^2})^{\frac{1}{2}} \int_{x_1}^{x_2}[V(x)-E]dx\} \tag{1.4}$$

where $V(x)$ and E are the electron's potential and kinetic energies; m is its mass, $\hbar$ the Planck's constant divided by 2π; x_1 and x_2 denote the edges of the potential barrier.

Müller and Tsong(5) assume an equilateral triangular potential barrier of height $(I-\sqrt[2]{e3F})$ and a base $(\frac{I-\phi}{eF})$. The maximum penetration probability in equation (1.4) corresponding to the critical distance x_c is given by

$$D(x_c) = \exp\{-4.55\times10^{-7}(I-7.60\times10^{-4}F^{\frac{1}{2}})^{\frac{1}{2}}(\frac{I-\phi}{F})\} \qquad (1.5)$$

The ionization probability is obtained by multiplying the barrier penetration probability with the frequency 'ν' with which the electron in the atom strikes the barrier. The lifetime before ionization is given by

$$T = \frac{1}{\nu D} \qquad (1.6)$$

The probability of ionization in a given time interval 't' can be expressed as

$$P(t) = 1-\exp(\frac{-t}{T}) \qquad (1.7)$$

Figure 1.4 shows a plot of the ionization probability of helium atoms as a function of the distance from a tungsten emitter for various fields.

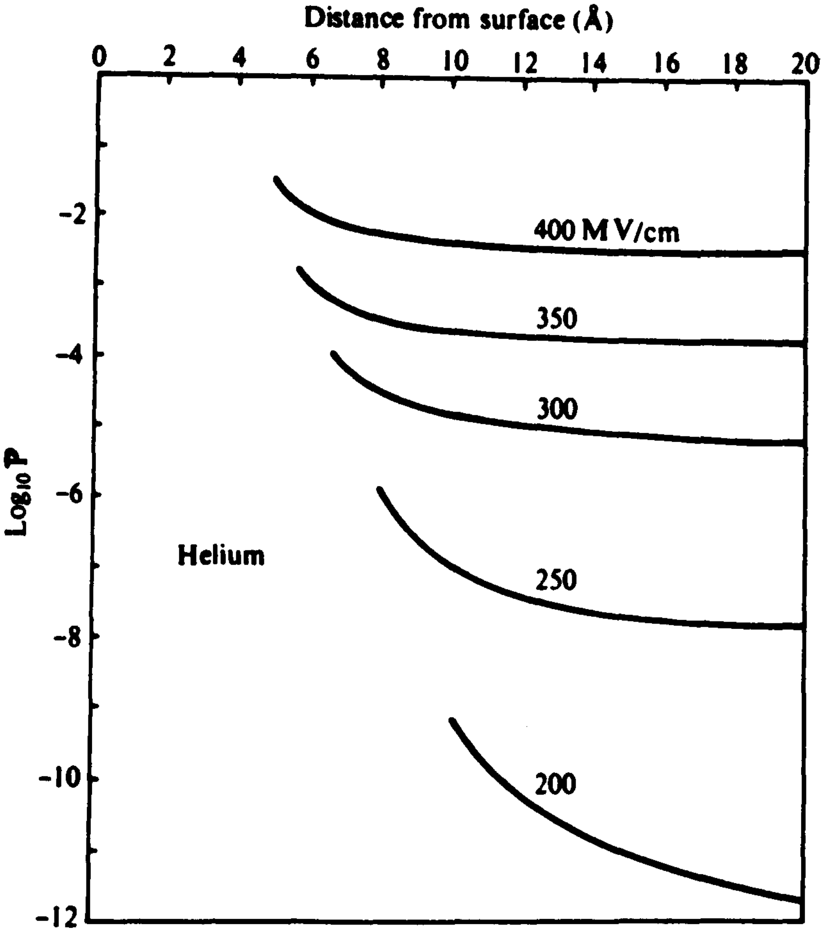

Figure 1.4 Field ionization probability of helium atoms(5).

It can be observed from figure 1.4 that the ionization probability is a very strong function of the applied field and also that the probability increases steeply just before disappearing at the critical distance x_c. This can be explained as being due to the great reduction in the potential barrier at short range through the electronic interaction with the surface as expressed by the image potential contribution.

Tsong and Müller(11) have measured the field ion energy distribution of helium ionized over a tungsten tip and find that ionization occurs within a very narrow region $\simeq$ 0.18 Å.

Knor and Müller(12) have proposed that field ionization models should include consideration of the interaction between the electron orbitals of the gas atom and those of the metal surface. They have suggested a molecular orbital model of the metal surface. Field ion images are interpreted as projections of regions where the fully occupied orbitals of the inert gas atoms can easily overlap with the partially occupied single or hybridized orbitals of the surface metal atoms. They have been able to explain regional image brightness, zone decoration, alternating ring contrast in HCP metals etc., on the basis of this model.

Moore and Brandon(13) also point out that crystallographic variations in brightness correspond to discrete changes in co-ordination number.

1.3.2 Field ion current

1.3.2(a) Ion current

The field ion current I may be expressed as(1)

$$I = ek_i n_t \qquad (1.8)$$

where e is the electronic charge, k_i is the ionization rate constant and n_t is the number of trapped gas molecules available for ionization. n_t can be defined as

$$n_t = \frac{Z}{k_i + k_d} \qquad (1.9)$$

where Z is the rate of arrival of gas atoms at the tip (to be discussed in detail later in this section) and k_d is the rate of escape of gas atoms by diffusion. The ion current is then

$$I = \frac{eZk_i}{k_i + k_d} \qquad (1.10)$$

At low fields, the rate of ionization is much less than the rate of diffusion ($k_i << k_d$), and the ion current can be expressed as

$$I = \frac{eZk_i}{k_d} \qquad (1.11)$$

At higher fields $k_i >> k_d$ and hence the ion current can be expressed as

$$I = eZ \tag{1.12}$$

corresponding to the prompt ionization of all gas atoms arriving at a rate determined by the supply function Z.

1.3.2(b) The Gas supply function

The gas supply function to the field ion emitter is calculated by approximating the emitter shape to a hemispherical cap on a cylindrical shank. The enhancement of gas supply due to the polarization of gas molecules in the presence of the field is also taken into account. Müller and Tsong(5) give the following expressions for gas supply function:

$$Z_s = 4\pi r^2 \frac{P}{(2\pi mkT)^{\frac{1}{2}}} \left(\frac{\alpha F^2}{2kT}\right)^{\frac{1}{2}} \tag{1.13}$$

for a spherical emitter where 'r' is the radius of the emitter, P is the gas pressure, T is the temperature of the gas, α is the polarizability and m is the atomic mass.

$$Z_c = 2\pi r \frac{P}{(2\pi mkT)^{\frac{1}{2}}} \left(\frac{2\alpha F^2}{\pi kT}\right)^{\frac{1}{2}} \tag{1.14}$$

for a unit length of cylindrical emitter of radius 'r'.

From empirical calculations of the gas supply(14), it is observed that a substantial portion of the gas atoms contributing to a typical field ion image initially strike the shank of the emitter, become trapped and are then drawn to the ionization zone at the apex of the emitter by polarization forces.

Müller(15) has developed the concept of 'hopping gas atoms' wherein the gas atoms perform a hopping motion on the surface of the tip before accommodation to the tip temperature.

1.3.2(c) Current voltage characteristics

The variation of Helium ion current with applied voltage for a tungsten emitter observed by Southon and Brandon(16) is given in figure 1.5.

The upper limit of the curve at D marks the onset of field evaporation. Initially, the ion current increases very sharply with the field as $(\text{Field})^n$, where $n \simeq 20$ to 40 and then a slow increase in ion current with the field in the region BCD. This suggests that above the point B, the ionization probability has saturated at a value corresponding to certain ionization of any gas atom near the emitter surface. Further increase in the field, leads to an increase in the gas supply due to increased polarization forces. Hence, the first portion of the curve is the region where the microscope operates in a strongly field dependant, ionization limited mode and in the region BCD, it operates in a field proportional, gas supply limited mode.

Figure 1.6 shows the effect of temperature on the current voltage characteristics. The evaporation field falls slowly with increasing temperature and the threshold field at which ionization starts to occur rises more rapidly with temperature. This observation implies that the emitter temperature affects the ionization probability by influencing the velocity distribution of the gas atoms,

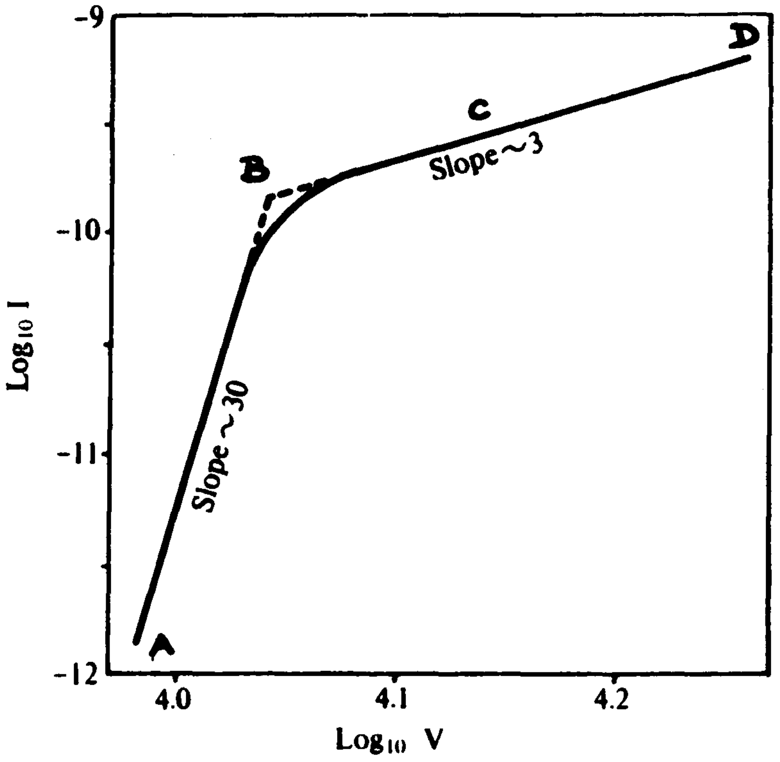

Figure 1.5 Typical variation of helium-ion current with voltage for a tungsten emitter at 77°K(16).

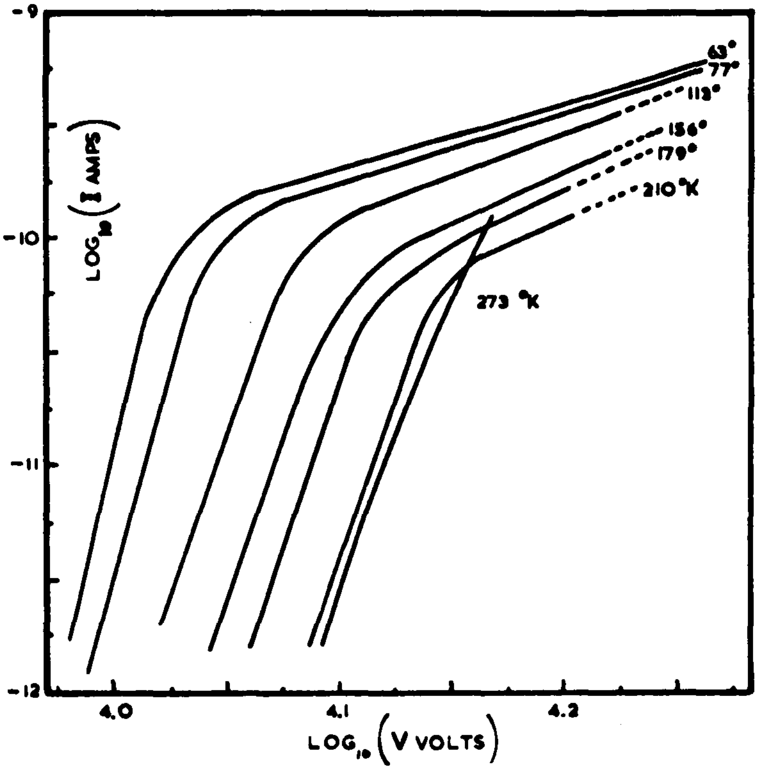

Figure 1.6 The current-voltage characteristics of a tungsten emitter of about 630 Å radius at various temperatures and at a helium pressure of 6×10^{-3} torr(16).

which determines the time for which an atom is present in the ionization zone.

The basic difficulty in explaining the actually measured current-voltage characteristics is the inhomogenity of the field over the emitting region. Not only is there a gradual decrease in the field towards the shank, also the radius of curvature of the tip cap over different regions varies widely. The protruding {111} regions of tungsten and the {102} regions of platinum already emit in the gas supply limited mode when the other regions of the emitter are still operating in the ionization limited mode. On the whole, the observed slopes of the current-voltage curves vary from emitter to emitter depending on the finer geometrical details of the emitter surface.

1.3.3 Magnification and Resolution

1.3.3(a) Magnification

In a point projection microscope like the FIM, the magnification η can be expressed as

$$\eta = \frac{R}{\beta r_t} \qquad (1.15)$$

where R is the tip to screen distance

r_t is the radius of the tip

β is a constant representing the image compression factor.

The above expression takes into account the fact that the emitter is not a freely suspended sphere providing an exactly radial projection. Normally the constant β is between 1.5 and 1.8 depending on the design of the microscope and the shape of the emitter(2).

1.3.3(b) Resolution

Assuming that the scattering of the field ions by the parent gas is negligible, the factors determining the resolution of the FIM may be considered under three headings: firstly, the extent to which the atomic structure of the emitter surface is reproduced as a spatial modulation of the electric field strength through a surface x_c above the emitter where the ionization predominantly occurs; secondly, the extent to which this modulation of the field strength produces a modulation of the ion current density leaving the emitter; and thirdly, the extent to which the spatial modulation of the ion current density above the emitter is retained in the ion beam reaching the fluorescent screen.

Only the third factor has been treated quantitatively(1,2). The image forming ions have a transverse velocity component normal to the direction of projection of the ions. This contributes to a loss of resolution on being projected to the phosphor screen. Diffraction effects also contribute to a loss of resolution. A particle localized within a distance parallel to the emitter surface has, from the Heisenberg uncertainty principle, a transverse velocity component. Again, ionization takes place over a finite area and this can be approximated by the radius of the image gas atom. Combining these three factors, the effective resolution can be expressed as(1)

$$\delta = \delta_0 + \left[\frac{2\hbar\beta r_t}{(2mev)^{\frac{1}{2}}} + \frac{16\beta^2 r_t^2 E_t}{ev}\right]^{\frac{1}{2}} \qquad (1.16)$$

where δ_0 is the radius of the image gas atom

$\frac{2\hbar\beta r_t}{(2mev)^{1/2}}$ is the diffraction contribution

where r_t is the tip radius and

v is the applied voltage

$\frac{16\beta^2 r_t^2 E_t}{ev}$ is the tangential velocity contribution where E_t is energy of the ion due to tangential velocity in the vicinity of the emitter.

δ_0 is about 1 Å for helium.

The contribution of the other two factors in equation (1.16) is about 1 Å for helium ionization at 21°K for a 1000 Å radius tip. Since the best possible resolution is between 2-3 Å, the modulation of electric field above the emitter surface must contribute to further loss of resolution.

As can be observed from equation (1.16) the best possible resolution is obtained by working with the smallest possible tip radius, accommodating the gas to the tip temperature before ionization and using a gas of high ionization potential, low polarizability and small atomic radius. These conditions make helium a very good choice as an image gas.

1.4 Field evaporation

Field evaporation(17) was first described as thermally activated evaporation of ions over the Schottky barrier(9) with an activation energy dependent on the applied field strength. In this section, field evaporation models based on thermal activation are outlined, followed by a survey of the modifications in the theory of field evaporation.

1.4.1 Image force theory

The representation of potential energies by one dimensional curves is assumed to be a fair approximation for the purposes of understanding field evaporation. The potential energy of an atom $v_A(x)$ as a function of distance x from the surface is shown in figure 1.7(a) where Λ is the sublimation energy of the atom. The energy required to remove a surface atom in the form of an ion, Q_o can be expressed as

$$Q_o = \Lambda + \sum_n I_n - n\phi \qquad (1.17)$$

where n is the charge on the ion

I_n is the n^{th} ionization potential

ϕ is the measured average work function of the metal

Figure 1.7(b) shows the potential energy of an ion approaching a metal surface. On applying an electric field, the potential energy of the ion will be reduced by a factor neFx where e is the electronic charge, F the applied field and x the distance from the metal surface. A maximum appears in the potential energy of the ion as shown in figure 1.7(c).

Neglecting the repulsion potential at sufficiently large distances, the potential energy of the ion can be expressed as

$$-V_I(x) = neFx + \frac{n^2e^2}{4x} \qquad (1.18)$$

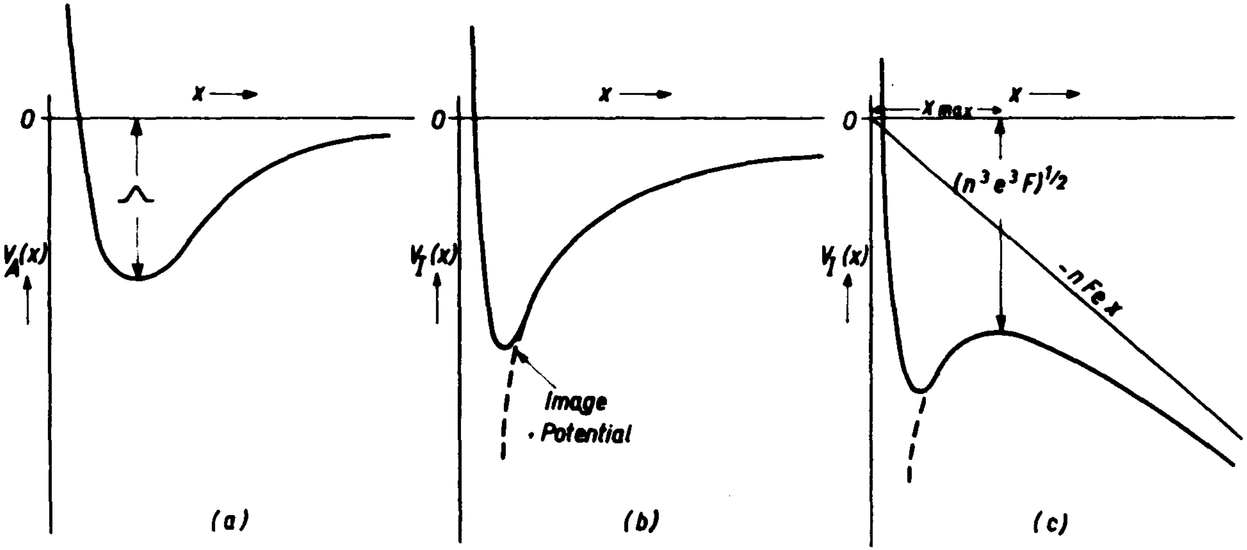

Figure 1.7 Potential energy curves (a) for an atom, (b) for an ion, and (c) for an ion in the presence of a field.

where $\frac{n^2e^2}{4x}$ is the attractive image potential of the ion and $neFx$ is the potential due to the applied field.

Differentiation to obtain energy maximum yields

$$\frac{1}{x_{max}} = \left(\frac{4F}{ne}\right)^{\frac{1}{2}} \qquad (1.19)$$

and

$$-V_{I(max)} = (n^3e^3F)^{\frac{1}{2}} \qquad (1.20)$$

This energy maximum is referred to as the 'Image' or the 'Schottky hump' and it is independent of x so long as the neglect of the repulsion potential implied by the equation (1.18) is justified. At a field of 500 MV/cm, the Schottky hump is only 0.85 Å for a singly charged ion and 1.2 Å for a doubly charged ion. This does not even allow for the radius of most ions. Hence, it is rather difficult to justify that an atom be thermally activated over the Schottky barrier.

1.4.2 Field evaporation models

Gomer and Swanson(18) have discussed the possible situations that may occur when the atomic and ionic potential curves are superimposed.

Firstly, if the ionization potential is sufficiently low, the ionic potential curve lies below the atomic potential curves and the species may be adsorbed on the surface as an ion; examples: cesium and barium on tungsten. Field evaporation occurs by vibrational excitation over the Schottky hump. (See figure 1.8(a))

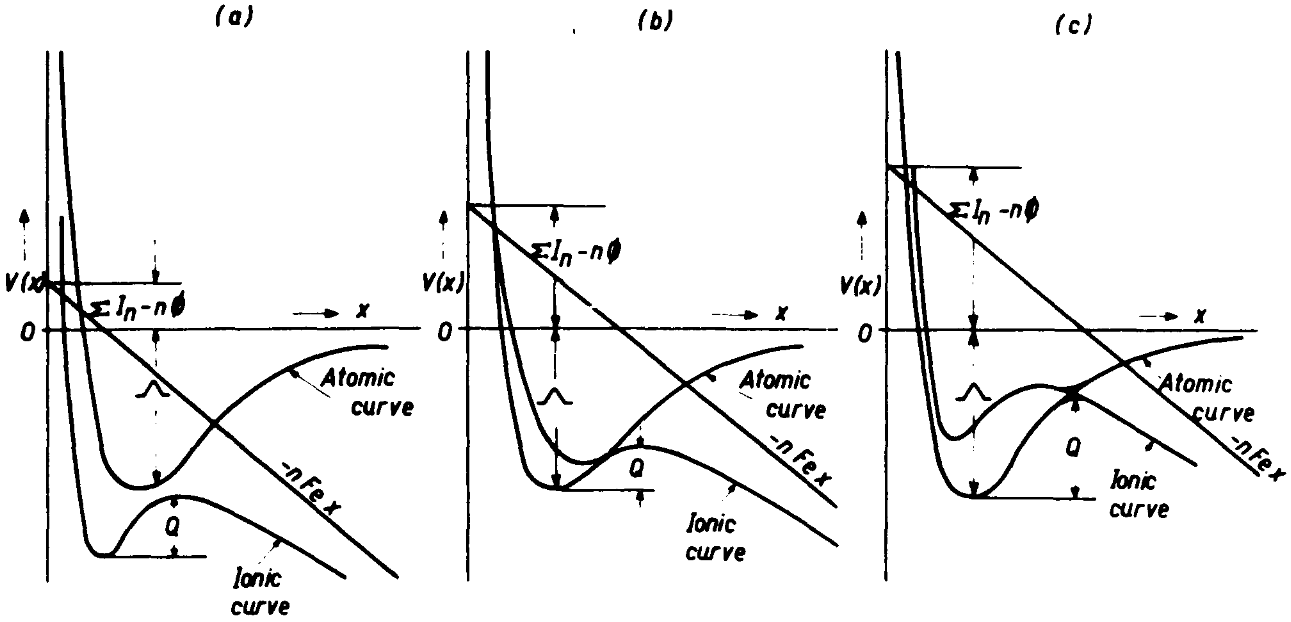

Figure 1.8 Superposition of potential energy curves (schematic) for (a) ionic state stable and (b) transition from atomic to ionic state, followed by evaporation over an image-potential hump, with (c) potential maximum at transition from atomic to ionic states(18).

Secondly, when the ionization potential is substantial, the atomic state is stable near the surface, but the ionic and atomic potential curves intersect to the left of the image hump. (See figure 1.8(b)). The minimum in the atomic potential lies $\Lambda + \sum_n I_n - n\phi$ below the zero of the ionic potential curve so that, the activation energy for field evaporation can be given by

$$Q = Q_o - (n^3e^3F)^{\frac{1}{2}} \qquad (1.21)$$

where $Q_o = \Lambda + \sum_n I_n - n\phi$ (1.22)

and $-(n^3e^3F)^{\frac{1}{2}}$ is the potential energy of the ion at the Schottky hump. This model of the field evaporation process where an ion is activated over the Schottky hump [figures 1.8(a) and (b)] is the 'image potential' model .

In a situation where the ionization potential is high enough so that the image hump lies above the atomic potential curve, the energy maximum corresponds to the intersection of the ionic and atomic potential curves (See figure 1.8(c)), and the activation energy is approximately given by (18,19)

$$Q = Q_o - neFx_c - \frac{n^2e^2}{4x_c} \qquad (1.23)$$

where x_c is the point of intersection. This is the 'intersection' model of field evaporation where the evaporation of an atom occurs at the instant of ionization.

Brandon(19) has considered the influence of the repulsion potential of the ion near the metal surface and concludes that if the repulsion potential is large, then it could reduce the image hump or even completely eliminate it in the extreme case. The activation energy is then given by equation (1.23). The repulsion term does not enter the equation because of the extremely short range of the force.

Brandon(19) has calculated the evaporation fields for various values of charges on field evaporating ions and suggests that the occurrence of doubly charged ions is quite likely. No definitive data is available on the ionization potentials of multiply charged ions but it is possible that more than doubly charged ions do occur. Tsong(20) points out that in the temperature range of interest to field ion microscopy, ionic tunneling cannot be neglected. Using the WKB approximation, he has calculated critical temperatures below which tunneling predominates.

1.4.3 Polarization effect

So far, the effect of the polarizability of the atom and the ion on the activation energy for field evaporation have not been taken into account. Consideration of this factor leads to an additional binding energy term given by

$$P = \tfrac{1}{2}(\alpha_a - \alpha_i)F^2 \qquad (1.24)$$

where α_a and α_i are the polarizabilities of the atom and the ion respectively. The differences in polarization energies associated with different planes are found to be more substantial than the differences in work functions, so that the orientation dependence of field evaporation might be more appropriately ascribed to the polarization factor than just the orientation sensitive work function(5). The polarization effect can be also thought of as a consequence of the field penetration or as a considerable lowering of the work function of the loosely packed planes.

1.4.4 Field evaporation end form

The binding energies of atoms vary with the crystallographic orientation. So, during field evaporation, the emitter retains its general shape through regionally specific evaporation rates such that regions with a high binding energy have a small radius of curvature and vice-versa. The overall radius of the tip increases with the progress of evaporation.

Field evaporation proceeds from sites which have a minimum value of Q, i.e. at the edges of net planes. But the polarization corrections and work function measurements are not representative of this location of an atom. The evaluation of the environmental conditions, such as the variation in binding energy due to foreign atoms, lattice defects,the number of bonds etc., is important.

Accounting for some of the geometric effects, the field strength effective at an evaporation site can be expressed as(21)

$$F = \beta_1 \beta_2 F_a \tag{1.25}$$

where $F_a = \frac{v}{kr_t}$ (1.26)

r_t is the average tip radius; v the applied voltage; k a constant, approximately equal to five(22); β_1 - the field enhancement factor to account for the smaller than or larger than average local radius and β_2 - a factor to account for the short range geometric effects such as the degree of protrusion of a lattice step and the presence of foreign atoms in the neighbourhood.

Computer simulation studies of emitter surfaces introduced by Moore(23) are very useful in quantitatively understanding the effects of complex factors such as lattice defects, domain structures, impurity atoms, alloying elements etc., on the field evaporation end form and image characteristics.

1.4.5 Effect of image gases

Field evaporation in the presence of an image gas leads to a reduction in the evaporation field and a change in the shape of the end form, depending on the image gas used(5). These two effects can be explained by understanding the state of the emitter surface. Firstly, the atom-probe studies have revealed that image gases are present on the emitter in an adsorbed state(7,24,25,26). Secondly, the desorption of molecular ions formed from the image gas and the surface metal atoms such as WHe^{+++}, WHe_2^{+++}, $I_rNe_2^{++}$ have been observed (24,25). The above knowledge of the gas metal surface interaction in conjunction with Knor and Müller's(12) molecular orbital model of the metal surface can explain the role of image gases in field evaporation(5).

The binding energy of the metal atom is reduced when a surface molecule is formed by the overlap of orbitals of the metal and the gas atoms. This reduces the evaporation field. The nature of the binding of the various image gases on different crystallographic regions determines the overall field evaporation end form.

In conclusion, it must be noted that the treatment of field evaporation as a thermally activated process has only been able to qualitatively explain the experimental observations. For example, atom-probe analysis of field evaporating ions(27-30) has confirmed the existence of multiply charged ions, earlier postulated by Brandon (19).

In spite of more complex treatments of field evaporation based on electronic transition(31,32) and a combination of thermal activation, electronic transition and ionic tunneling(20), a sound theory has not been formulated. This is probably due to the lack of reliable concepts of the electronic condition of the metal surface in the presence of extremely high fields.

1.5 Image Interpretation

1.5.1 Indexing and the radius of curvature

The relative positions of the various crystal planes in field ion micrographs depend on the geometry of the field ion microscope and on the tip shape. The type of projection portrayed in field ion micrographs can generally be approximated as being stereographic, although the projection in different areas of a micrograph differ due to differences in radii over different crystallographic regions of the tip(1).

The assumption of stereographic projection greatly simplifies interpretation. However, caution must be exercised in drawing quantitative conclusions based on the stereographic projection.

The sizes of the planes in field ion micrographs are approximately proportional to the surface atom densities of the planes(33). The radius of curvature of an emitter can be accurately calculated by counting the number of net rings between two poles of known angular separation(33).

1.5.2 Regional image brightness and zone decoration(12).

The electron orbitals of atoms emerging at the surface represent partially occupied states. The image gas can be ionized when its wave function overlaps with that of the broken bond, giving rise to an image spot. The borken bonds themselves could interact with those of the neighbouring atoms and thus form complete bonds. Such sites do not give rise to image spots on the micrograph. This explains the alternating ring contrast in h.c.p. metals. This concept of surface orbitals when applied to different crystallographic areas of emitter surfaces of various metals can explain the relative brightness patterns observed in practice. The outer electronic configurations of metals may be the cause of the differences in the ion images of different metals of the same crystal structure.

The extra brightness and broader image spot size of the zone line decoration atoms(34) can be attributed to the fewer orbitals being occupied because of the protruding sites they occupy on the emitter surface.

1.5.3 Distribution of surface charge

The presence of a different atomic species on an emitter surface leads to a rearrangement of surface charge due to interactions between the two atomic species(12,35,36). This partially empties the surface states around one of the atom species and this charge redistribution leaves these atoms more positively charged. On the application of the field, these atoms experience an enhanced field above them,thus increasing the ionization probability. The above model satisfactorily explains the hydrogen promotion effect and contrast of oxygen interstials in various metals(36). The most important application of the concept of charge redistribution is in the interpretation of alloy images.

1.5.4 Artefacts

Defects may be introduced in the specimen or eliminated as a result of the tip preparation technique, the high surface to volume ratio and the stress on the tip due to the imaging field. Massive streaking of images is usually observed if the specimen preparation technique is not proper(37,38,39) or if the specimen is heavily deformed(40). Zone decoration lines (explained earlier) are artefacts caused by the field stabilization of atoms in metastable sites (1). Points on the screen where the phosphor is damaged and dim image spots which are below the light level for the photographic emulsion may give the impression of a vacant lattice site(1).

Tip preparation by electrolytic etching may cause an estimated 20% reduction om dislocation density(41). The dislocation configurations may change due to the large surface area/volume ratio and the imaging field stress(1). The field stress can cause homogenous nucleation of dislocation loops(42) or mechanical twinning(43).

1.5.5 Observation of defects

Bowkett and Smith(44) have given an extensive review of field ion microscope studies in the area of lattice defects. The identification of point defects is fairly straight forward. As for dislocations, stacking faults and partial dislocations it must be mentioned that a spiral contrast is to be expected.

1.5.6 Determination of grain boundary parameters

The orientation relation between two grains can be described in terms of an axis and angle of rotation as described below(44). This method assumes that the image is a stereographic projection. Hence, the method described is not accurate, but provides a rapid way of estimating grain misorientations.

The approximate position of the grain boundary is determined by visual inspection. Three pairs of field ion poles having the same indices with one pole of each kind in grain A and one in grain B are constructed on a stereogram. Three great circles are constructed, one inclined equally to each of the three pairs of poles. The axis of rotation M is given by the intersection of these great circles. The angle of mis-orientation 'α' can be determined by the angle between the poles of the great circles through M and $(hkl)_A$ and, M and $(hkl)_B$.

Determination of the grain boundary plane(s) necessitates the use of approximation which makes the procedure rather inaccurate. In the idealized case, a plane intersecting a spherical surface would give a small circle in the stereographic projection. The pole of this small circle would be the pole of the intersecting plane. In practice, this procedure may be far from simple because, the tip is not a spherical cap and the grain boundaries are not always planar and the projection is not exactly stereographic. Nevertheless, the above method can be applied to small lengths of the grain boundary trace in regions of constant local radius.

Another method(45) is to calculate the inclination of the boundary to the specimen axis by noting the movement of the trace of the grain boundary during a known amount of field evaporation. This method gives better accuracy, but entails a lot of work.

1.5.6-a Low angle grain boundaries

The contrast from a single perfect dislocation emerging in a pole with normal 'n' is 'p' interleaved spirals where 'p' is the resolved component of the Burgers vector 'b' in 'n' measured in units of appropriate interplanar spacings(46). When more than one dislocation is enclosed, the spiral configuration depends on the sum of the Burgers vectors enclosed and spirals of unexpected multiplicity can be produced. Figure 1.9 is a sketch of the multiple spiral effect produced by a sub boundary emerging in a field ion tip.

1.5.6-b High angle grain boundaries

Within the accuracy of this technique, Mott's island model(47) and the coincidence site lattice theory(48) with extensions(49) have been shown to be in fair agreement with the observation of grain

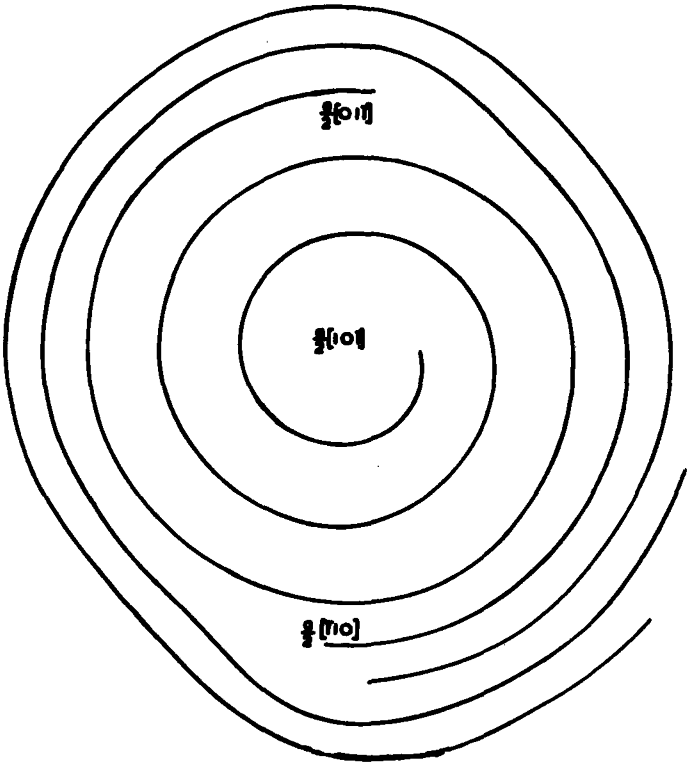

Figure 1.9 Sketch illustrating the type of multiple spiral effect produced by a sub-boundary emerging in a field ion tip.

boundary structure in metals(48,49,50), whereas, Loberg et al.(51) do not agree with the coincidence site lattice model of grain boundaries. Ring configurations observed in field ion images of high angle boundaries in tungsten have been attributed to the presence of dislocations(52). The same configurations could be produced by the relative orientations of the planes meeting at the boundary(51,53).

Field ion observations suggest indirectly that the width of grain boundaries is of the order of one or two atomic diameters. The term 'indirect' is used because small displacements of the order of one quarter of the Burger's vector may not be easily detected in the field ion microscope. The correlation between misfit and high energy leading to preferential evaporation(48) is not always true because of the complexities of the imaging process(53). The topology of grain boundaries has been studied in detail and found to consist of a number of facets(54). The field ion microscope has not yet provided much information about atom configurations at grain boundaries, mainly because of the difficulties in interpreting the images and in finding the grain boundary parameters accurately.

1.5.7 Contrast from alloys

At present there is a controversy over the interpretation of alloy images. There are two factors to be considered. (i) The evaporation behavior of the solute atom, i.e., preferential evaporation or preferential retention. (ii) The imaging characteristics, i.e., bright or invisible in spite of being present in the lattice.

The above effects occur basically because of the electronic charge transfer(35,36) that occurs when a solute atom is present in a matrix of solvent atoms. This charge redistribution in the presence of the electric field accentuates the differences in electronic charges around the surface atoms and leads to enhanced field around the species that is more positively charged compared to the neighbours.

The first factor to be determined is, which one of the two atomic species involved is the one that accepts electronic charges and which is the one that parts with some of the electronic charge. Several criteria are available to decide the direction of electron transfer between atoms. Southworth and Ralph(55,56) have chosen the work function values to represent closely the situation existing on metal surfaces. The other criteria are ionization potential and electronegativity. Using the work function criterion for charge transfer and a modified field evaporation theory for solutes in a solvent matrix, Southworth and Ralph(55,56) have been able to convincingly explain most of the field ion observations of alloys(57,58) as being due to 'preferential evaporation' of the solute species.

Tsong and Müller(59,60) and Tsong(35,61) object to this interpretation because solute atoms inside closely packed planes could not be field evaporated preferentially. They have tried to explain the invisibility of certain species in alloy systems as being due to 'selective ionization' atop the surface atoms. In trying to explain the various observations, they have had to invoke many criteria such as the shielding of one species by another, size effect, position in the periodic table, effects of outer electronic configuration etc. Knowing the complexities involved in the electronic structure of metal surfaces under the high electric field, it is not surprising that many obscure factors are involved in imaging. Though the 'preferential evaporation' model of Southworth and Ralph seems attractive, a great amount of caution must be exercised in interpreting individual systems because, most of the concepts used in this model - field evaporation of solute atoms in a solvent matrix, polarization binding of atoms etc., are not quantitatively predictable and could at best be rough estimates.

It must be pointed out that the interaction of the image gas with the atomic species on the emitter surface could play an important role in determining the field evaporation end form and the field-ionization behaviour of alloys in the FIM. Such an effect has been acknowledged in the case of pure metals(5,12). Only atom-probe studies of various alloy systems can improve our understanding of FIM images of alloys.

CHAPTER 2

THIN FILMS

2.1 Introduction

The nucleation and growth of thin films has been reviewed by Pashley(62). The subject of thin films is dealt in this chapter with particular reference to field ion microscope studies of thin films.

2.2 The preparation of thin films

Evaporation technique is usually employed in the preparation of thin films the deposit source being activated by resistive heating. Though numerous vapour deposition experiments have been done under moderate vacuum conditions (10^{-5}-10^{-7} torr)(62), field ion/field emission microscope studies of vapour deposited films have always been conducted under ultra-high vacuum (less than 10^{-9} torr)(63,64,65).

Field ion emitters can be cleaned by a combination of heating and field evaporation thus providing a fairly clean substrate for deposition. The topography of field ion emitters is ideal for studying the orientation dependence of different aspects of film growth and for observing the structure of interfaces between the deposit and the substrate in different crystallographic regions. Heating of the substrate during and after deposition is favourable for obtaining large crystals of the deposit and for epitaxial growth(62). Controlled field evaporation of the deposit is very convenient for a detailed structural observation of the deposit and the interface between the substrate and the deposit. The thickness of the deposit can generally be obtained from field evaporation data.

The above mentioned features of field ion microscopy, which are ideally suited for the study of thin films, along with the tremendous resolution and magnification afforded by the imaging process make FIM a very powerful tool for research in this field.

The only drawback of field ion microscopy is the extremely high stresses involved during imaging and field evaporation.

2.3 The nucleation and growth of thin films

Pashley(62) in his review on thin films has reported a number of cases where isolated three-dimensional nuclei were randomly distributed with no preferred sites for nucleation. Field electron emission studies of copper on tungsten(63,64) have distinctly shown preferred sites for nucleation of copper on tungsten surface - the preferred sites being the {001} and {111} planes and the {011} plane edges.

On the basis of the experimental observations presented in his review, Pashley(62) has concluded against the possibility of psuedomorphic growth of deposits on substrates of a different crystal structure. On the other hand, Jones(63) has noted that the first four to six monolayers of the deposit were constrained to the substrate lattice (i.e. pseudomorphic) and that further deposition led to the formation of deposit crystallites with normal bulk structure. The existence of such 'transition layers' has been confirmed by

Melmed(64) and by the combined field ion and field electron emission studies of gold on tungsten by Montagn-Pollock et al(65). More recently Smith and Anderson(66) and Moss and Blott(67) have observed the existence of constrained 'transition layers' in their study of nickel on tungsten and copper on tungsten respectively. All the above evidence is in contradiction to the conclusion of Pashley(62) on the existence of pseudomorphic layers.

Whitmell(68) has conducted the only study so far on thick vapour deposited films. He has obtained epitaxial deposits of iridium on molybdenum with the following orientation relationships

$$(111)_{Ir} \quad || \quad (110)_{Mo}$$

and $$[10\bar{1}]_{Ir} \quad || \quad [1\bar{1}1]_{Mo}$$

He has reported the presence of stacking faults in the deposit. He also observes that the interface between iridium and molybdenum was only one or two atoms thick, with the initial layer of iridium assuming the molybdenum structure and being firmly bound to the molybdenum substrate. Rendulic and Müller(69), have observed thick electro-deposited films of platinum on iridium and tungsten. They report that the deposit crystals were mainly [111] oriented.

2.4 Alloying during deposition

Bassett et al.(70) have reported formation of alloys at temperatures below that required for substantial bulk diffusion, whereas, Whitmell$^{(68)}$ has reported no alloy formation up to 900°C in the Ir-M_o system.

CHAPTER 3

INTERPHASE BOUNDARIES

3.1 Introduction

In this chapter, the discussion is restricted to the subject of interphase boundaries observed in solid state alloy systems.

One of the principal factors responsible for the evolution of precipitate morphology in diffusional phase transformations is the structure and the consequent migrational characteristics of the interphase boundary separating the precipitate crystal from the matrix phase. Smith(71) has classified interphase boundaries in the following manner:

1. Incoherent (disordered) boundaries: have isotropic structures and possess high mobility at elevated temperatures due to rapid and independent transfer of atoms across or along these boundaries.

2. Partially coherent (dislocation) boundaries: are made up of uniformly spaced arrays of dislocations. Appreciable volumes of the lattices on both sides of the boundary are strained. Accumulation of volume strain energy is the major restraint to the advancement of this type of a boundary.

3. Coherent boundaries: contain no dislocations and strain substantial volumes of metal about them. There is no mechanism available for their movement. The restraint is the accumulation of volume strain energy.

3.2 Incoherent or disordered boundaries

The energy of a disordered boundary should be effectively independent of the orientation of the boundary. Hence, such an interphase boundary between a precipitate and the matrix should be more or less smoothly curved. The interface is assumed to be such that a dislocation description is impossible, but Malcolm and Purdy (72) have observed facets at the tips of Kurdjumow-Sachs related Widmanstätten α-plates in β Cu-Zn. These facets were of the semi-coherent type and corresponded to approximately (335) in the f.c.c. α matrix. Aaronson et al.(73) have cited instances where semi-coherent areas were present at disordered interfaces.

The migration of disordered boundaries should generally be at rates allowed by volume diffusion control(74). Many instances where the migration of disordered boundaries were faster than or slower than permitted by volume diffusion control have been reported (73). The faster migration rate could possibly be attributed to interfacial diffusion(75), whereas, the slower migration could be due to solute drag effects(76) or probably the formation of semi-coherent segments at the boundary.

Overall, the exact atomic structure of disordered interphase boundaries and their migrational characteristics in relation to their structure is not clearly understood. Direct observation of the structure of disordered interphase boundaries in the field ion microscope would be of great interest in the present context.

3.3 Partially coherent or dislocation boundaries

The energy of dislocation boundaries as a function of misfit have been calculated(77,78,79,80) assuming cubic crystals of parallel orientation for the sake of simplicity in treatment. The most important results of these treatments can be summarized as (i) misfit energy increases rapidly with misfit when the misfit is less than 10%, (ii) at larger misfits the dependence of misfit energy on the magnitude of misfit is negligible, (iii) about 98% of the energy is stored within a distance equal to half the thickness of the boundary, (iv) a coherent interface structure is stable until a critical value of misfit is exceeded. In the b.c.c./f.c.c. interface, Brooks(80) notes that the inter-dislocation spacing will be too close for any meaningful dislocation discription of the interface. Paxton(81) objects to the dislocation description on similar grounds and suggests a mechanism by which coherency can be attained over a substantial area of the interface by sub-lattice translations of the atoms at the interface. Aaronson(82) has proposed a ledge model for the description of dislocation boundaries and has had some sucess with it in describing interfaces such as the broad sides of Widmanstätten plates. In this model, the planar faces of the ledges are amenable to dislocation description, whereas the edges of the ledges are assumed to be of the disordered type. Experimentally, the misfit compensating efficiencies of the dislocations were rather poor and the arrays of dislocations were not of a minimum energy configuration. These have been explained as being due to the activation energy required for the nucleation of equilibrium dislocations(73).

Flewitt(83) has observed regular dislocation arrays possibly of the type $\frac{a}{6}<112>$ on the planes bounding Widmanstätten 'α' needles in β-brass. Researchers at the Ford scientific laboratory(84) have observed large spaced dislocations on (nominally) planar interfaces in the Cu-Cr system. The interface has been modeled as a sequence of steps whose broad faces are formed by $\{110\}_{b.c.c.} \parallel \{111\}_{f.c.c.}$ Most of the misfit between the lattices has been accommodated by restricting the extent of the steps to regions of good fit and they suggest that the large spaced interfacial dislocations serve to eliminate the residual mismatch. The habit planes expected on the basis of their model is $\{335\}_{f.c.c.}$ for the Cu-Cr system, which is the same as that observed earlier by Malcolm and Purdy(72) in the Cu-Zn system.

The mobility of such ledged interfaces seems to be diffusion controlled(73). Here again a wide variation has been reported(73). This is probably due to the heterogenous structure of different dislocation boundaries. Even an individual interface could exhibit a considerable range of heterogenity in structure. There is an added possibility of dislocation configuration at the disordered edge of the ledges. The contribution of pipe diffusion along dislocation lines could be one of the factors for the discrepancies observed in the migrational characteristics of dislocation interfaces.

On the basis of the evidence presented in this section, it can be concluded that the current understanding of partially coherent interfaces is not sufficient to explain all the observations on the basis of a unified theory. It is hoped that a systematic study of such interfaces at a high resolution would throw some light on the true situation existing at such interfaces. Unfortunately, no quantitative theory has been proposed for complete characterization of two phase interfaces observed in the FIM. The only attempt generally in that direction is that of Howell et al(85).

CHAPTER 4

EXPERIMENTAL

4.1 Design of an all-glass high vacuum FIM

An all-glass FIM was designed to operate under liquid nitrogen cooling and helium gas imaging. The design was mainly oriented toward easy tip and screen replacements. Hence, greased ground-glass joints were used instead of awkward glass blown joints or costly flanges required for an ultra-high vacuum microscope. (See figure 4.1).

4.1.1 The Vacuum System

This consisted of a 3-stage mercury diffusion pump and a titanium getter pump, backed by a 2-stage oil sealed mechanical rotary pump. With efficient trapping of mercury vapours by three liquid nitrogen traps, the system was kept fairly clean. The microscope head was positioned between a tall liquid nitrogen trap which acted as a cryo-pump on the one side and a titanium getter pump immersed in liquid nitrogen on the other. The pressure measurement was done by a Granville-Phillips ionization gauge head mounted on the side arm of the microscope, as shown in figure 4.1 and a Balzer's ionization gauge controller unit IMG-2 which was sensitive in the range of 10^{-3} torr to 10^{-8} torr. The pressure measurements using this arrangement could be taken to be fairly representative of the actual pressure near the field ion emitter. A thorough degassing of all the metal parts inside the system, coupled with an efficient use of the cold traps and the

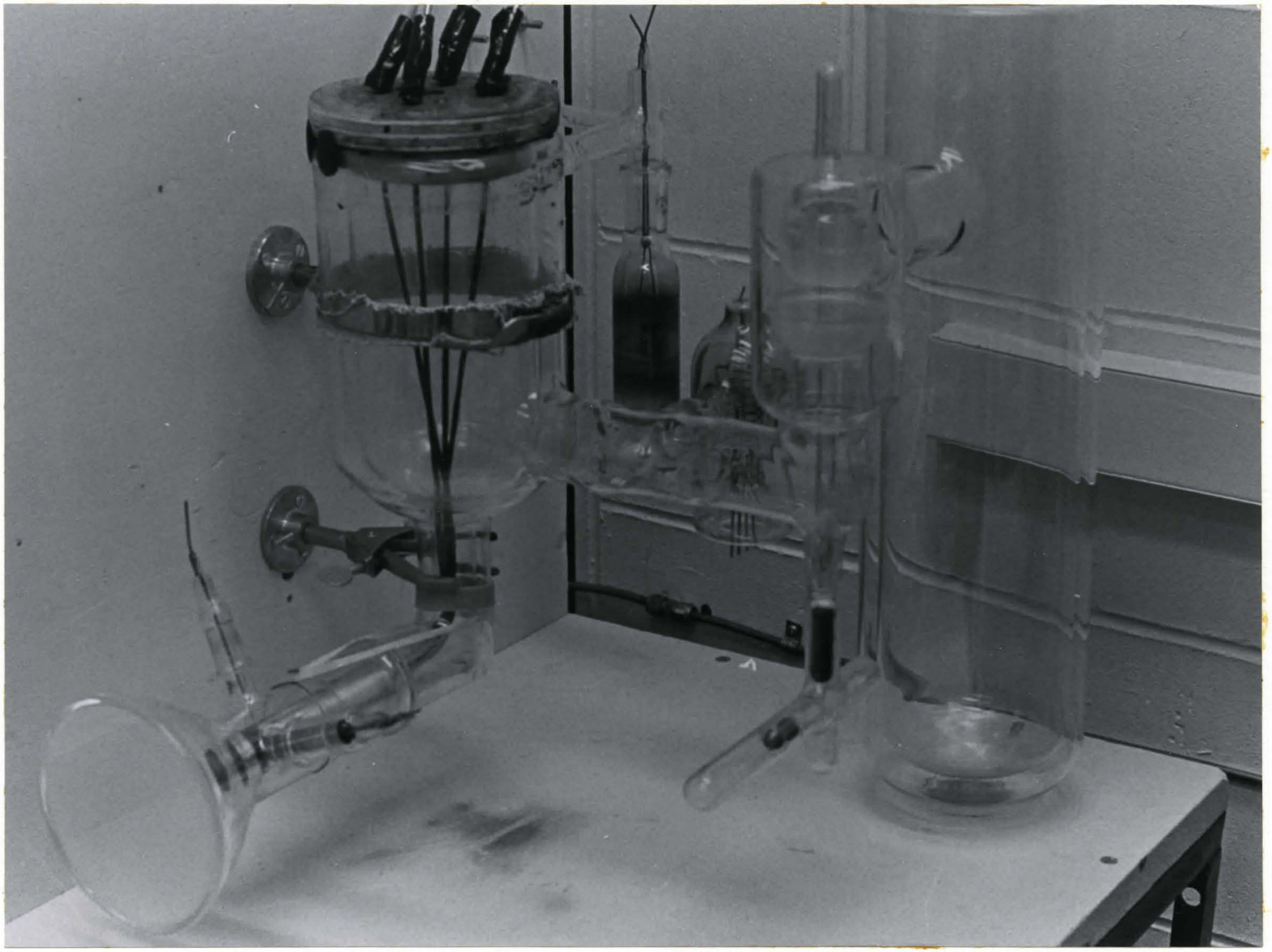

Figure 4.1 A photograph of the field ion microscope designed for the present work.

titanium pump always ensured a vacuum better than 3×10^{-8} torr.

4.1.2 The microscope chamber, the specimen holder and the screen

The microscope head was a simple double walled dewar of about 2 litres capacity. No elaborate measures were taken to cut radiation losses to save on the cost of the refrigerant. Filling half the dewar with liquid nitrogen, lasted for over an hour. The top was closely fitted with a wooden disc having provisions for filling liquid nitrogen and for connecting the leads from a 4-lead press-seal with the external circuit. The electrical connections were very well insulated to prevent any sparking during operation.

A 4-lead press seal was used in this design to facilitate in-situ tip heating and temperature control. The specimen holder was a bent 0.010" dia. tungsent wire spot welded on stainless steel cylinders which fit tight on the press-seal leads, thus ensuring a good thermal contact (fig. 4.2). Two more such wires could be connected up for temperature measurements.

The distance from the specimen tip to the screen was about 7.5 cms and the screen diameter about 11.0 cms. The size of the screen was very well suited for recording on 35 mm film and 4:1 image size reduction with commercially available large aperture objective cameras. The screens were prepared by dust settling the phosphor on the flat glass coated with a thin uniform layer of phosphoric acid in methanol. The phosphor used for preparing the screens was Sylvania Phosphor, type 160.

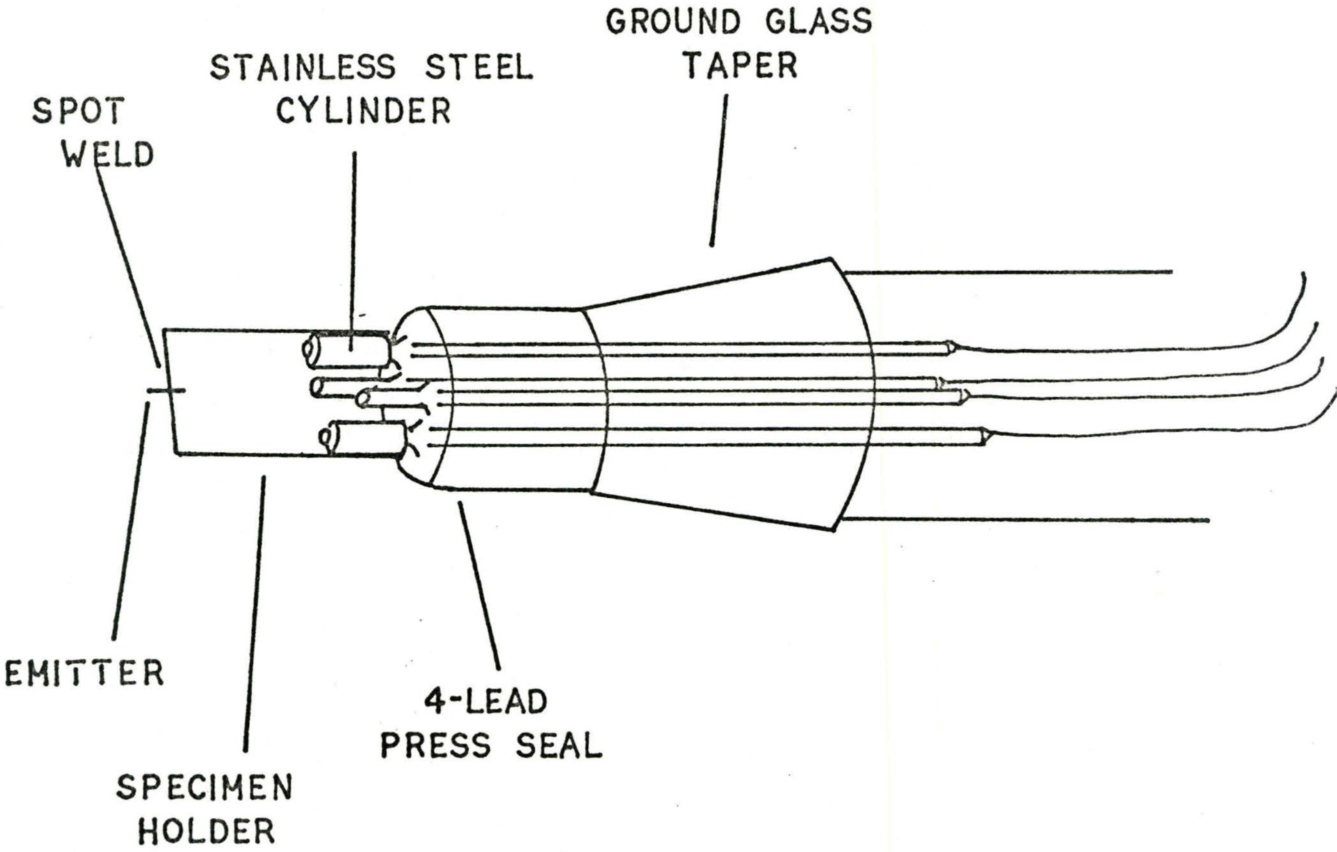

Figure 4.2 Tip assembly.

4.1.3 The image gas

Helium of spectroscopic purity was used as the image gas. The gas pressure during operation was kept at 3-4x10^{-3} torr.

4.1.4 Specimen coolant

Liquid nitrogen (boiling point 77°K) was chosen as the specimen coolant partly because of its cost free abundant supply at this university. Some of the other advantages of liquid nitrogen are: simplified design of the microscope head; no danger of explosion (as with liquid hydrogen) and a satisfactory resolution. To cool the image gas surrounding the specimen, a precisely machined aluminum mantle (figure 4.3) was slipped on a tapered ground glass joint just above the 4-lead press seal (figure 4.2).

4.2 Accessories

4.2.1 High voltage supply

A Universal Voltronics high voltage supply, model BRE-30-2AM rated at 30 KV DC and 2mA, with less than 0.01% r.m.s. ripple voltage was used. Positive voltage was applied on the tip while the screen was held at ground potential through a thin layer of tin oxide coating on the inside of the screen.

4.2.2 Pulse field evaporation circuit

A pulse field evaporation circuit facilitates a clear viewing of the image while the emitter surface is being field evaporated by short, frequent voltage pulses. The circuit used for this purpose is sketched in figure 4.4. A Universal Voltronics high voltage supply

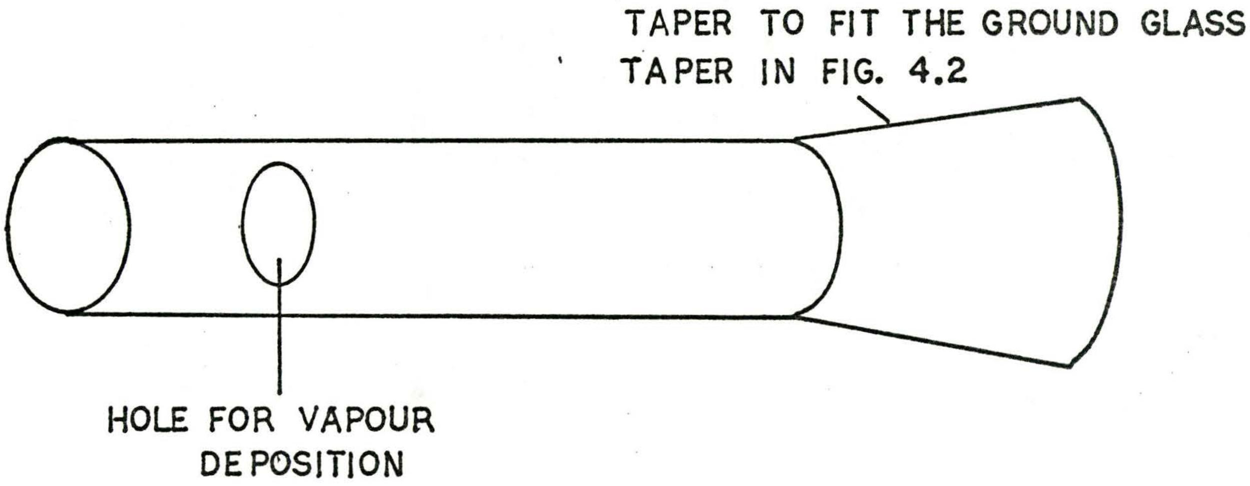

Figure 4.3 Aluminum mantle.

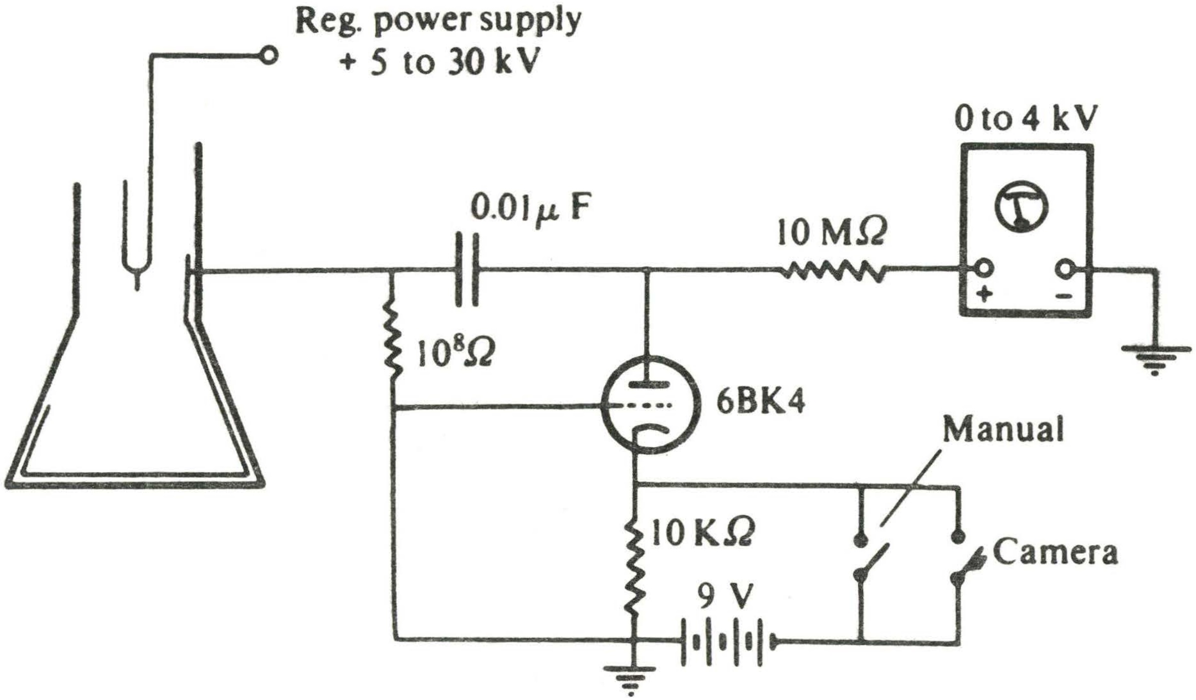

Figure 4.4 Pulse field evaporation circuit$^{(5)}$.

model BAM-10-5.5 rated at 10 KVDC and 5.5 mA with 1.5% r.m.s. ripple voltage was used in the circuit.

4.2.3 Tip heating circuit

A constant current power supply rated at 10 A maximum heating current was used for this purpose. This in conjunction with a Kelvin double bridge circuit could be used for controlled heating of the tip. The bridge was not in commission at the time of the experiments and hence, the temperatures were estimated by visual inspection.

4.2.4 High voltage isolation switch

A plexi-glass isolation switch was designed to connect the leads from the 4-lead press seal in the microscope to the high voltage supply in one position and the tip heating circuit in the other.

4.2.5 Metal vapour source

This consisted of a 0.010" diameter iridium/platinum wire coiled and spot welded on the leads of a press seal (figure 4.5). The wires used were 99.995% pure.

4.2.6 Power supply for the metal vapour source

This was a simple variac-transformer circuit capable of putting out a maximum of 10 A heating current.

4.3 Photography

The field ion image spots are very weak and it takes very good dark adaption of the eyes to observe them. The flat glass screen used in this FIM design facilitated the use of large aperture lenses with a very small depth of focus for photographing such weak images. The

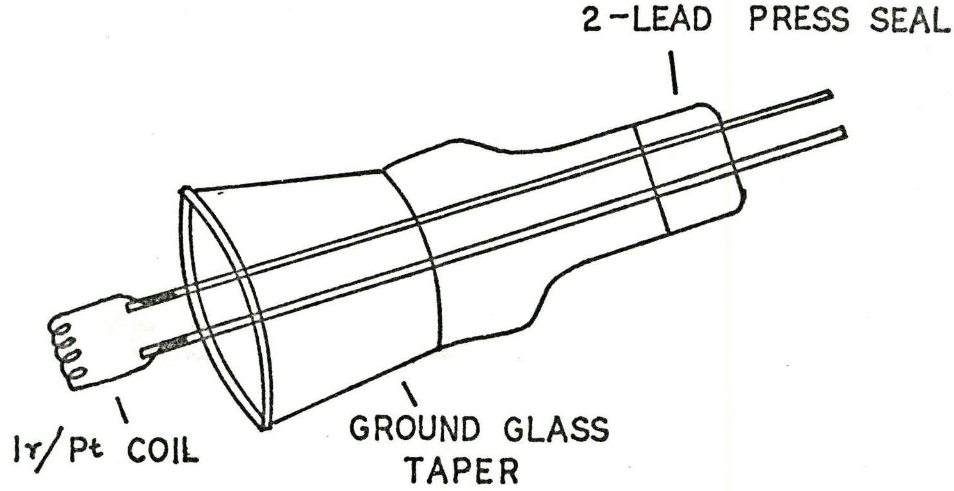

Figure 4.5 Vapour source.

The camera used was an Asahi Pentax SL with a f 1.4, 50 mm lens, with an image reduction ratio of 4:1. The camera was mounted on a side arm on the supporting structure of the microscope and could be swung into position in front of the screen for taking exposures. Due to the small depth of focus, the focussing of the camera on the phospor grains was very critical. The film used was Kodak Tri-X-pan which, when developed in Acufine diluted 1:1, gave a speed of 1200 ASA. An empirical plot of the exposure time versus the best image voltage is given in figure 4.6.

4.4 Tip preparation

The starting material was a 0.003" diameter tungsten wire (Philips Elmet Co.). This stock was found to be very pure in field emission observations. A short piece of the wire was spot welded on the specimen holder. Field ion tips were prepared by electrolytic etching of the wire. The electrolyte was made up of one part by volume of KOH (45%) and three parts by volume of aqueous NH_4OH. Graphite was the inert electrode. The voltage used was about 1.5 V A.C. The etching was carried on until the specimen was about 3-4 mm long. The tip was subsequently observed under an optical microscope with 800 magnification to speculate on its performance as a field ion emitter.

4.5 An experimental run

A freshly prepared specimen was mounted on the 4-lead press seal. The aluminium cone was then slipped on the ground joint.

Figure 4.6 An emperical plot of the photographic exposure time versus the best image voltage.

Proper alignment of the specimen and the cone was ensured. Then the screen was placed in position with a tight fit at the greased ground glass taper joint. The system was then pumped by the rotary and diffusion pumps which generally brought the pressure down to about $5x10^{-6}$ torr. Then all the metal parts were degassed at temperatures well above their working temperatures. The tall liquid nitrogen trap and the titanium pump were filled with liquid nitrogen in that order. Activation of the titanium pump a few times and the filling of the microscope head with liquid nitrogen usually resulted in a vacuum better than $3x10^{-8}$ torr.

The titanium pump and the microscope head were valved off from the pumps. The required pressure of helium was then leaked in. The camera was mounted on the side arm and accurately focussed on the phosphor grains. After allowing at least 10-15 minutes for dark adaptation of the eyes, the high voltage was turned on. Field evaporation end form was achieved by carefully field evaporating the emitter. Then the voltage was adjusted to the best image voltage and an exposure taken.

After photographing the clean tungsten substrate, the system was opened to the pumps, once again attaining a pressure of $2\text{-}3x10^{-8}$ torr. The high voltage was then turned off. The leads were connected to the tip heating circuit through the isolation switch. The tip was first heated to the required brightness and then the metal vapour source was activated. After deposition the tip temperature was adjusted to the required annealing temperature. After annealing the deposited tip for the required length of time the image gas was once again admitted and tip was imaged.

The annealing times and temperatures were varied; so also the substrate temperatures during deposition and the rates of deposition. These data are quoted in the next chapter. The background pressure during deposition were up as high as 5×10^{-7} torr. The pressure during annealing was in the $2\text{-}5 \times 10^{-8}$ torr range.

CHAPTER 5

RESULTS AND DISCUSSION

5.1 Analysis of a high angle grain boundary

The micrograph in figure 5.1 shows a high angle grain boundary observed in a 360 Å radius tungsten field ion emitter. Figure 5.2 is a stereographic plot of the micrograph in figure 5.1. A few prominent poles are plotted in the stereogram along with the trace of the grain boundary plane. The crystals can be described as having a rotation of 25 ± 3° about an axis M (in figure 5.2) which is close to the [110] axes in both the crystals. In addition there is a few degrees (4-6°) twist and tilt about axes orthogonal to the axis M.

The grain boundary in this case is not entirely planar (as shown by the trace in figure 5.2). A major portion of the boundary PQ, appears planar, the pole of the boundary plane being approximately $(3\bar{1}5)_A$. There appears to be a small jog QR, 8-10 Å high followed by another plane facet RS which probably is again a $(3\bar{1}5)_A$. The part ST of the grain boundary has not been indexed because of the inaccuracies involved in indexing short lengths of planes visible in field ion micrographs. The faceted appearance of this grain boundary is similar to that reported by Bayuzick and Goodrich(54). The coincidence relation closest to the present situation is a 26.5° rotation about the [110] axis which would give a reciprocal density of common points $\Sigma=19$. The planes having the highest density of common lattice points would be the {133} planes. A tendency of the grain boundary to

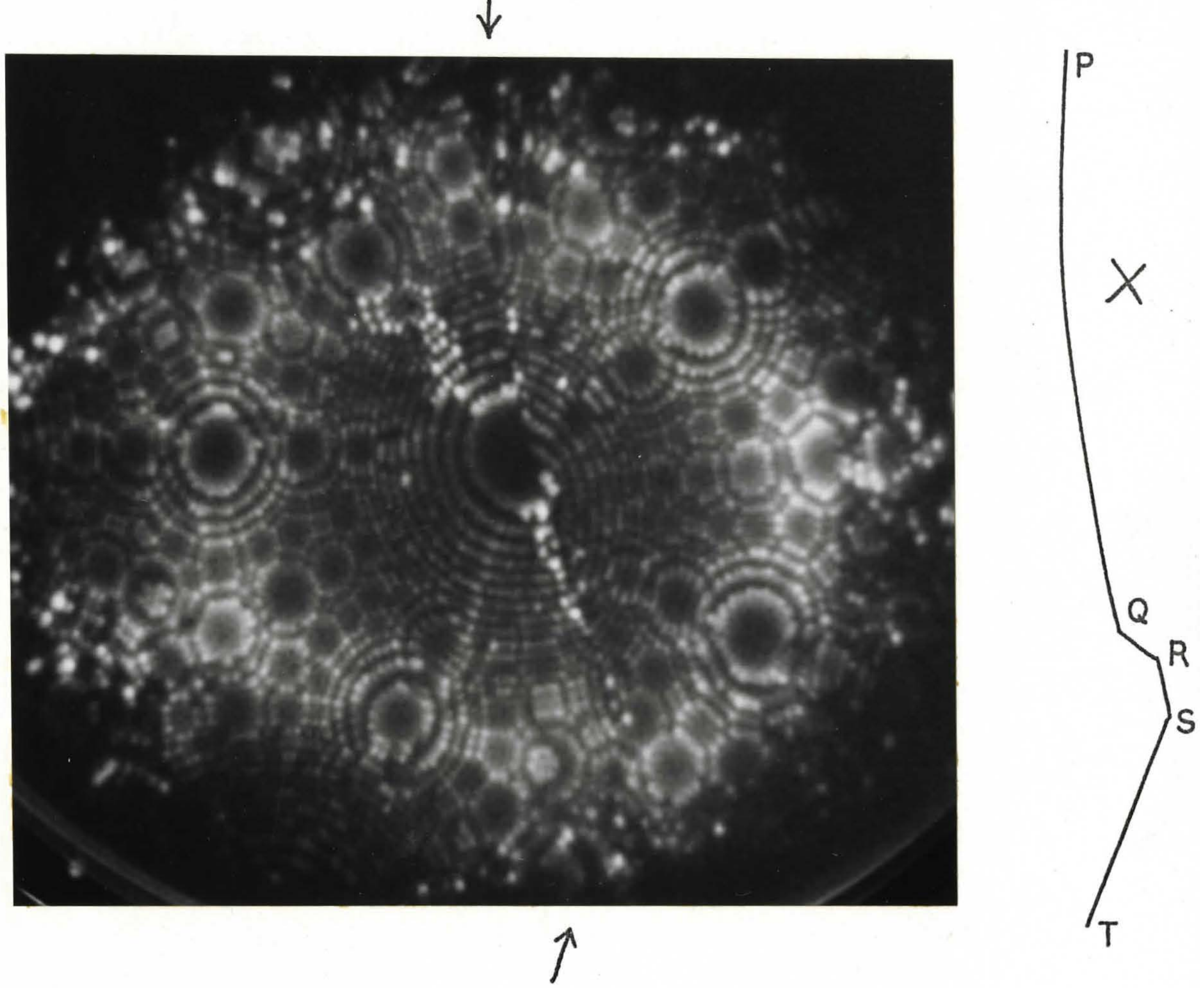

Figure 5.1 Field ion micrograph of a high angle grain boundary observed in a tungsten emitter. The trace of the grain boundary is sketched alongside.

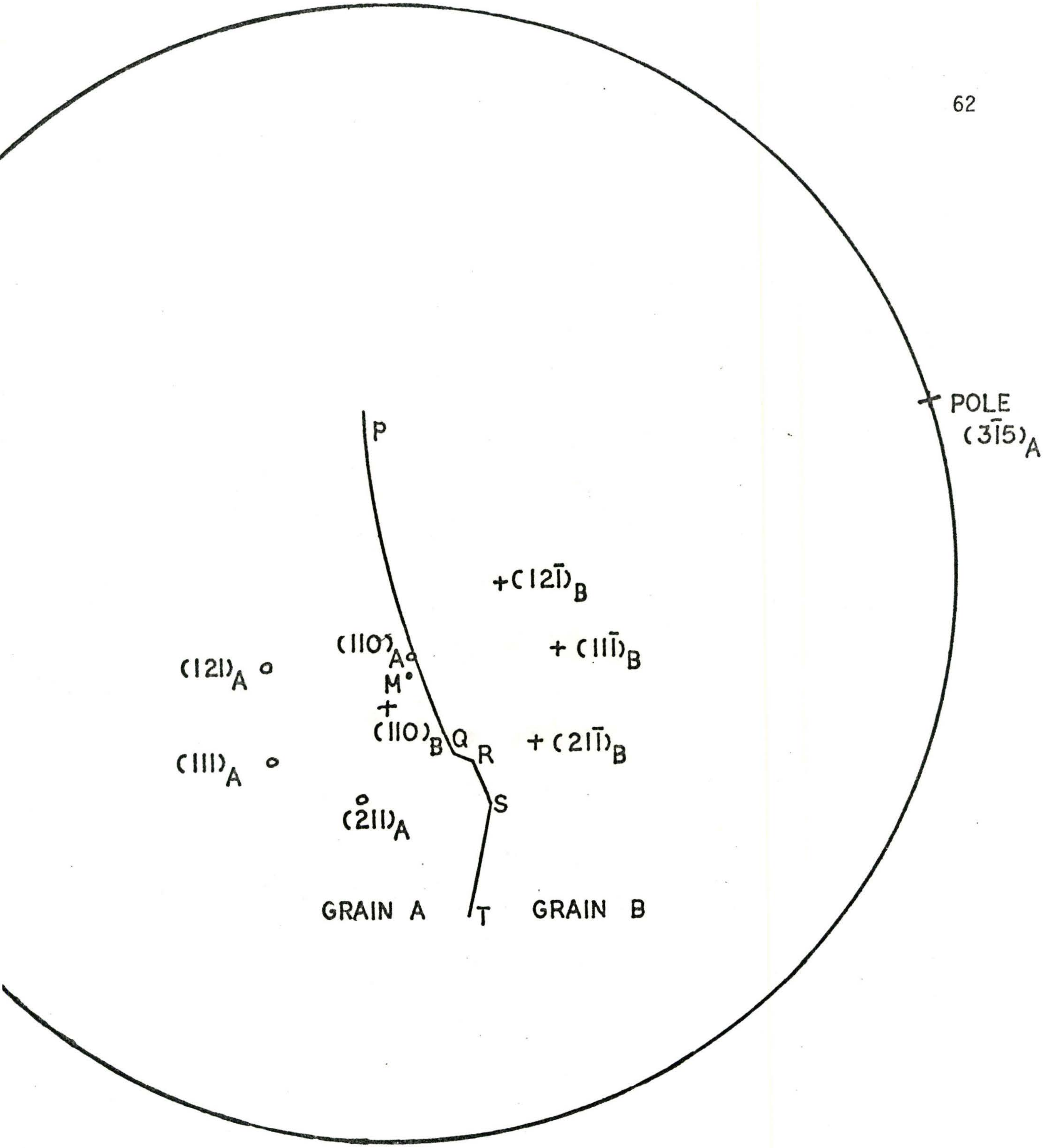

Figure 5.2 A stereographic plot of the micrograph in figure 5.1.

follow the {133} planes is not observed probably because the grain boundary is not in its lowest energy configuration. A closer look at the details of the interface structure which follows, gives us an idea of the locations of the atoms at the interface.

In spite of the large misorientation between the two crystals, there appears to be a generally good fit across the interface. In the region QR there is a smooth continuation of the ring structure across the interface, whereas in the region RST the structure is rather disordered. The spiral configuration observed in the region PQ is probably due to the few degrees twist associated with the boundary. The ring structure on either side seems to terminate abruptly at the interface at points in between the rings from the other side. Such a contrast could be produced by a small relative translation of one of the crystals along the axis of rotation M, or by a discrete change in magnification across the boundary.

The most striking feature of this boundary is the constrained bending of the (110) rings in crystal A to match four rings of crystal A with five rings from across the interface at the point marked X in figure 5.1. The observation of such a configuration suggests sub-lattice translation of atoms near the interface to obtain registry across the interface. The possibility of an artefact causing such a contrast can generally be ruled out. Hence, in spite of the limited resolution of the microscope (2-3Å), it is possible to detect relative translations of the order of an angstrom or less, under suitable conditions.

It is apparent from the micrograph in figure 5.1 that the comparative resolution (i.e. the resolution obtained by comparing the positions of atoms at different sites with the positions expected in a normal lattice) of the field ion microscope is better than an angstrom and that this potential can be exploited in obtaining detailed information on the structure of twins, stacking faults, grain boundaries, two phase interfaces and other crystal defects.

It must be noted that the occurrence of a grain boundary in field ion images is a rare event and grain boundaries were observed only in two instances out of the series of experiments conducted. Also, the stability of such emitters is unpredictable. In the case of the grain boundary reported here, the specimen fractured soon after the image was recorded.

5.2 Vapour deposition experiments: Choice of the systems

In the vapour deposition experiments conducted, attempts were made to grow platinum (f.c.c.) and iridium (f.c.c.) epitaxially on tungsten (b.c.c.) substrates. The choice of the system platinum-tungsten was governed by the ease of imaging platinum and tungsten in helium at 77°K, the similarity of lattice constants and their alloying behaviour. (Most of the relevant data on platinum, iridium and tungsten are given in table 5.1.) Platinum and tungsten have limited solid solubility in each other(86), which is a definite advantage. The only intermediate phase that exists is an ordered WPt_3(?) whose crystal structure is not known(86). The comparatively lower melting point of

Table 5.1

Metal	Crystal Structure	At. No.	n.n. distance Å	Percent misfit on close packed rows	Melting point °C	Work function	Electro-negativity
Tungsten	BCC	74	2.734	-	3410	4.52	1.7
Platinum	FCC	78	2.775	1.5%	1769	5.32	2.2
Iridium	FCC	77	2.714	0.6%	2454	5.0	2.2

platinum would require a lower temperature anneal for attaining epitaxy. The use of lower temperatures generally rules out the chances of any large scale surface rearrangement of the tungsten substrate and alloying between platinum and tungsten.

After several unsuccessful attempts to obtain a crystalline deposit of platinum on tungsten, iridium was tried in place of platinum. The main advantages of using iridium are the better stability or iridium field ion images, lower misfit between close packed rows of iridium and tungsten and the existence of an ε phase (h.c.p.) of known composition(87). The disadvantages are the fairly large solubility of tungsten in iridium and the high melting temperature of iridium which necessitates the use of higher substrate temperatures during annealing for the crystallization of the deposit and the attainment of epitaxy, thus increasing the chances of a large scale thermal rearrangement of the tungsten surface.

5.3 Deposition of platinum on tungsten

Deposition of platinum vapour on tungsten was done at slow rates (about one layer a minute). The substrate temperature was held at 800-850°C and very little annealing was done before imaging the deposited surface. The average thickness of the deposit was about 6-10 layers. The following micrographs are representative of the general nature of the deposits obtained under the stated conditions.

The micrographs in figures 5.3 (a) and (b) show the clean tungsten substrate and the platinum deposit on the substrate respectively. (The arrows in all the figures indicate the direction of the

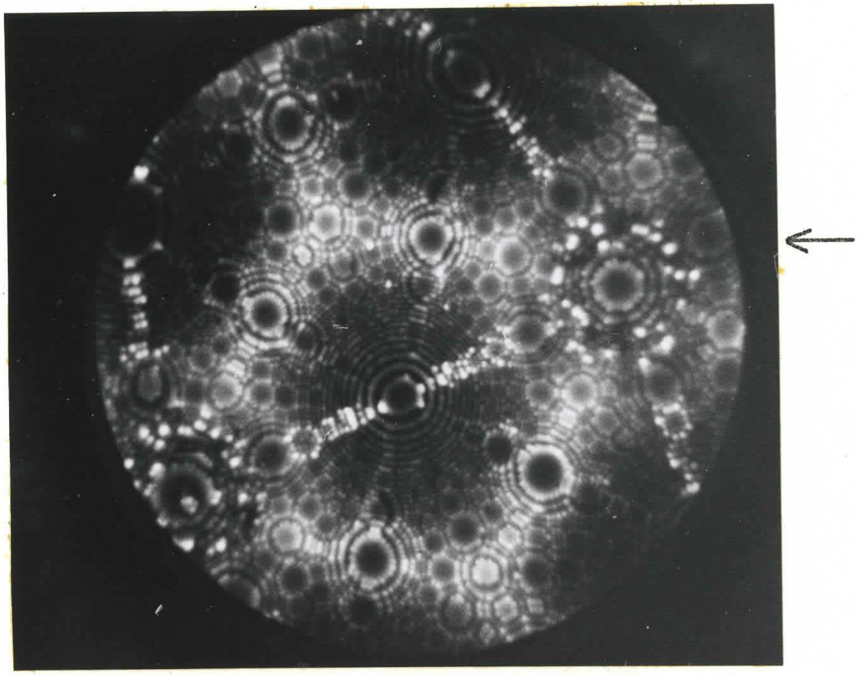

Figure 5.3 (a) Tungsten substrate. BIV 11.0 KV

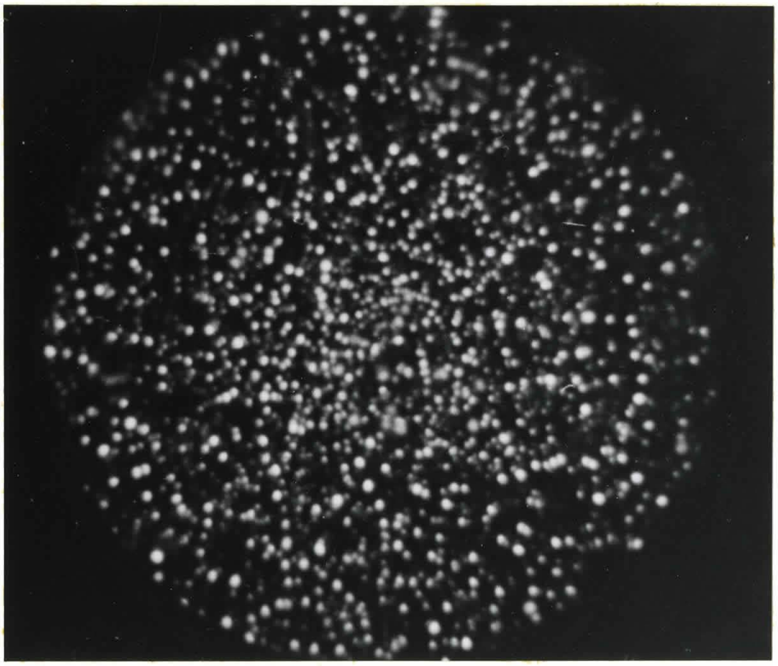

Figure 5.3 (b) Image of the platinum deposit on the substrate. Note the ring forming tendency in the deposit corresponding to $(110)_W$. BIV 11.0 KV

incident vapour flux.) The deposit in figure 5.3 (b) is structure less over most areas of the micrograph with some ring forming tendency around the central (110) region. (The formation of perfect net plane rings is taken to be indicative of complete crystallinity of the material).

Figures 5.4 (a) and (b) represent respectively, the clean tungsten substrate and the deposited surface after the removal of some of the deposit by field evaporation. In figure 5.4 (b) the left hand side shows a thermally rearranged tungsten surface whereas the deposit is still left on the right hand side showing a bright dot contrast similar to the deposit in figure 5.3 (b). Note the ring like structure corresponding to the (100) tungsten.

The experimental conditions, i.e., low vapour flux, moderate vacuum and the absence of annealing are probably responsible for the nature of the deposits seen in figures 5.3 (b) and 5.4 (b). The contaminant atoms arriving at the tip during deposition probably outnumbered the platinum atoms leading to the formation of a structureless random mixture of contaminant atoms and platinum atoms, which field evaporated randomly. Turnbull(88) has observed the amorphous structure of metal/metalloid compounds such as Au_3Si, Ni_5P and identifies these as 'metallic glasses'. In the present case, it is possible that the substrate and deposit atoms and the contamination (i.e. carbon, nitrogen, oxygen, hydrogen etc.,) have combined to form an amorphous 'metallic glass'.

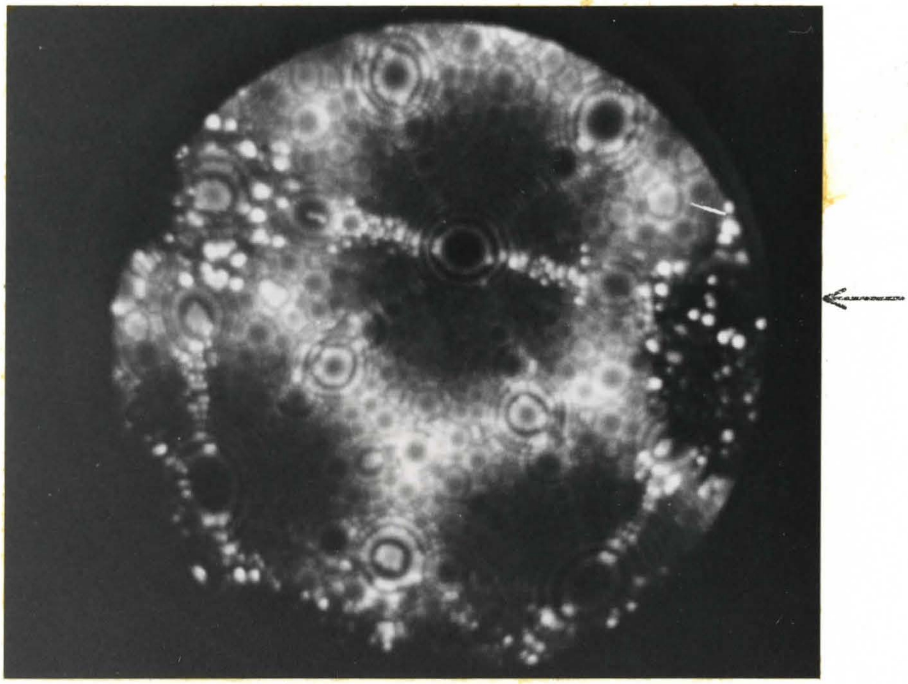

Figure 5.4 (a) Tungsten substrate. BIV 11.7 KV

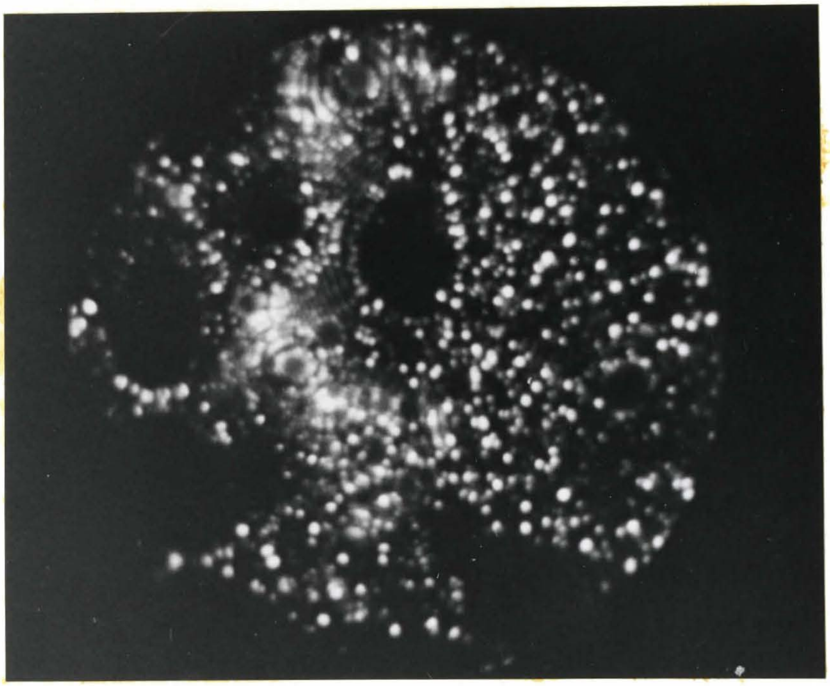

Figure 5.4 (b) The substrate is partially uncovered after some field evaporation. Note the ring structure in the deposit corresponding to $(100)_W$. BIV 10.7 KV.

In these experiments, it should be noted that the ring forming tendency in the deposit is observed in areas corresponding to prominent substrate planes.

5.4 Deposition of iridium on tungsten I

In this set of experiments, iridium was vapour deposited on tungsten at low vapour fluxes (about 2 layers a minute) and annealed at different temperatures for various times. Two typical experiments out of the several performed are presented below. As a rule, the substrate temperature during deposition and annealing, was kept the same.

Figure 5.5 (a) is the micrograph of the tungsten substrate on which iridium was deposited for 30 minutes and subsequently annealed for 2 hours at 800°C. Figures 5.5 (b) and (c) show the structure of the deposit at different stages of field evaporation. The ring forming tendency in the deposit is noticeable at several locations, though the basic contrast of the deposit is itself the same as for the platinum deposit (section 5.3). The deposit seems to be fairly thick (as observed from the differences in the image voltages quoted in the figures). No improvement in the structure is noticeable as the deposit/substrate interface is approached by continued field evaporation (see figure 5.5 (c)). The deposit was annealed for a further 75 minutes at 800°C with no change in structure. The deposit in figure 5.5 (c) seems to be more or less evenly spread on the substrate surface.

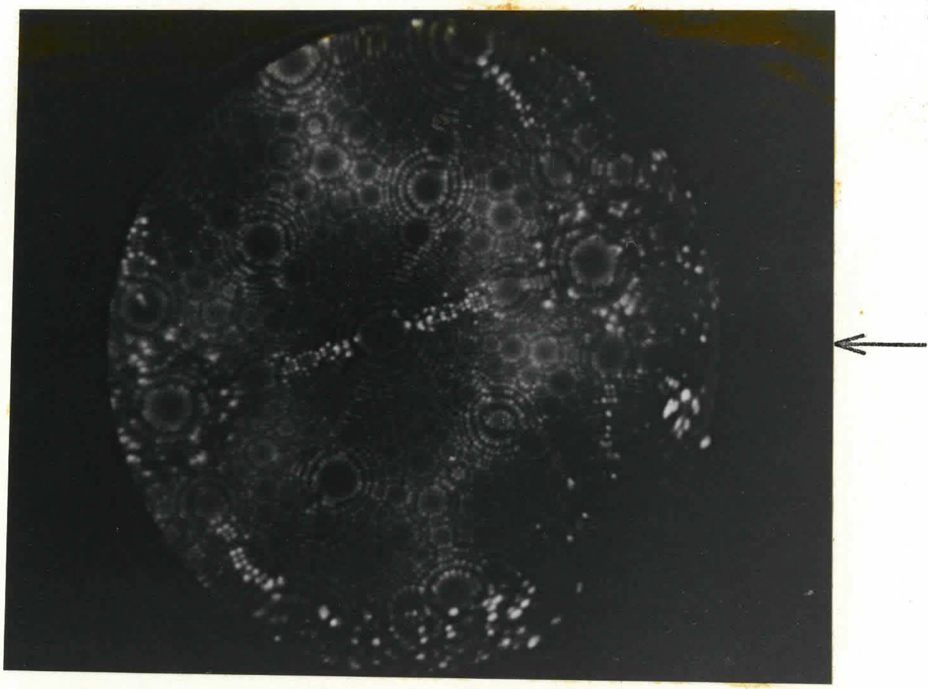

Figure 5.5 (a) Tungsten substrate. BIV 12.7 KV

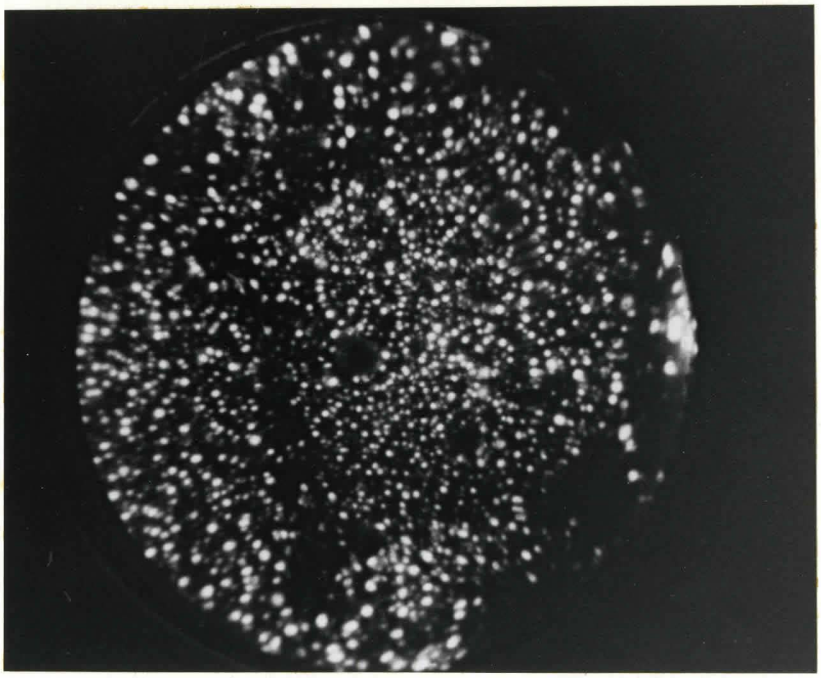

Figure 5.5 (b) Iridium deposit on the substrate. Note the development of ring structure at several locations. BIV 11.7 KV.

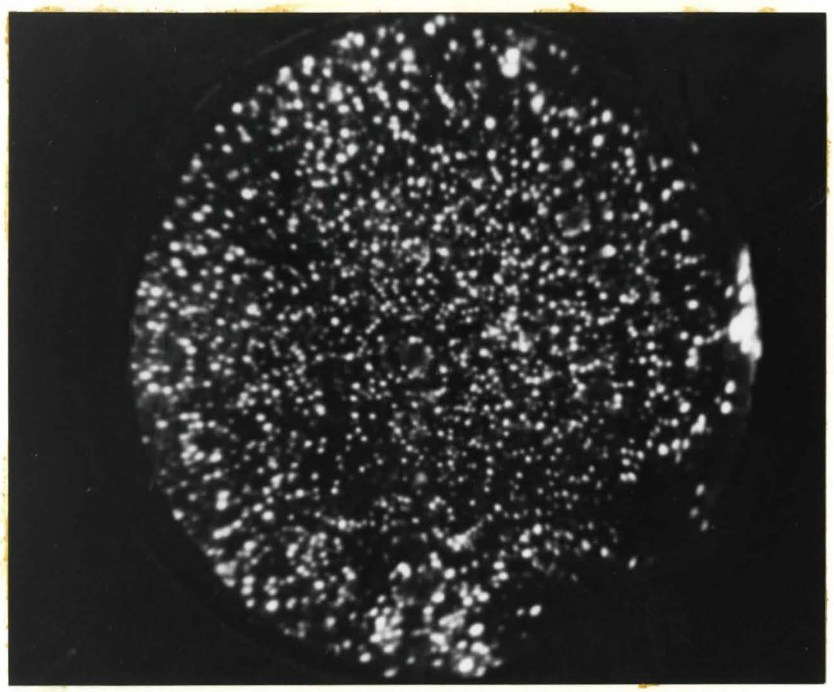

Figure 5.5 (c) The deposit after further field evaporation.

BIV 12.5 KV.

Figure 5.6 (a) shows the tungsten surface on which about 15-20 layers of iridium were deposited at 900°C and subsequently annealed for 2 hours followed by a high temperature anneal (1050°-1150°C) for 20 minutes. The micrograph of figure 5.6 (b) shows a fairly clear interface between the deposit and the substrate. The deposit still has an amorphous appearance, with a few irregular rings developed at different locations. Figure 5.6 (c) shows the surface after further field evaporation. The interface has receded. A prominent feature of the deposit is the ring structure centered on the ledges of the central (110) plane of tungsten. The only comment that can be made on this interface is that it is made up of small steps 10-15 Å wide. Since the deposit is not crystalline, no significant conclusions can be drawn.

The noticeable differences between this set of experiments where the deposit was annealed and the previous set where very little annealing was done (section 5.3) are: (i) the deposit is fairly stable against field evaporation (ii) irregular ring structures are developed at random locations without any preferred tendency to form rings centered on prominent poles in the substrate.

It should be noted that the ring structure observed in these deposits appear similar to the ones observed in disordered alloys(56). Considering the high annealing temperatures involved, the possibility of alloy formation cannot be entirely discounted(70). However, because of similarities to previous results (section 5.3) where there is less chance of alloy formation, it can be generally concluded that the

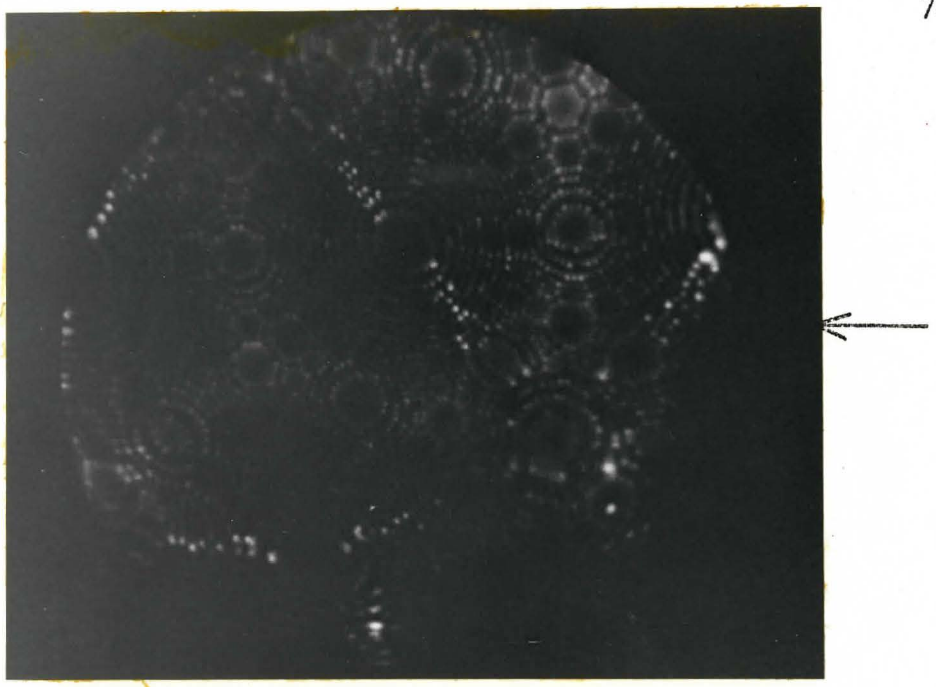

Figure 5.6 (a) Tungsten substrate. BIV 8.5 KV.

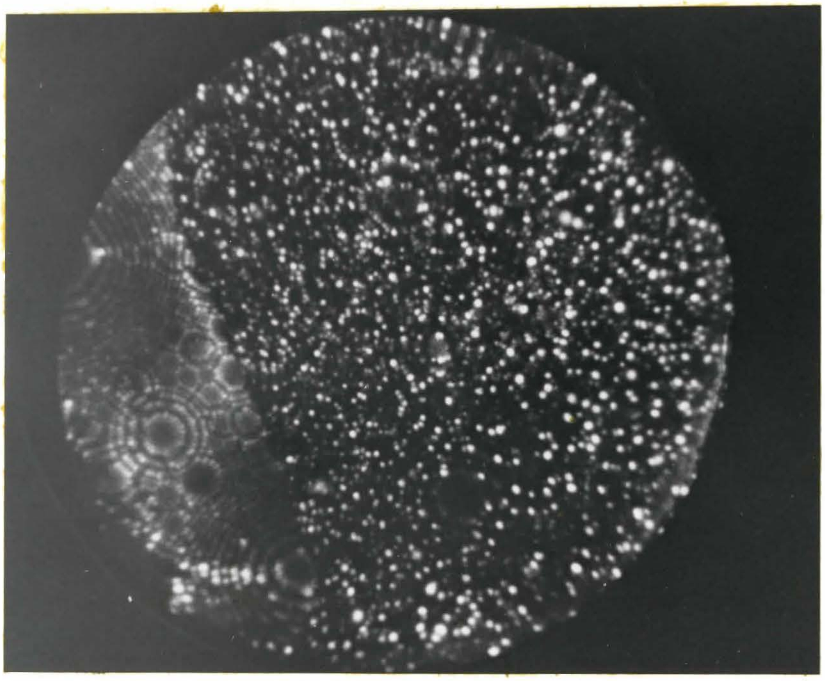

Figure 5.6 (b) Iridium deposit on tungsten after annealing. A clear interface between the deposit and the substrate is visible. BIV 13.0 KV.

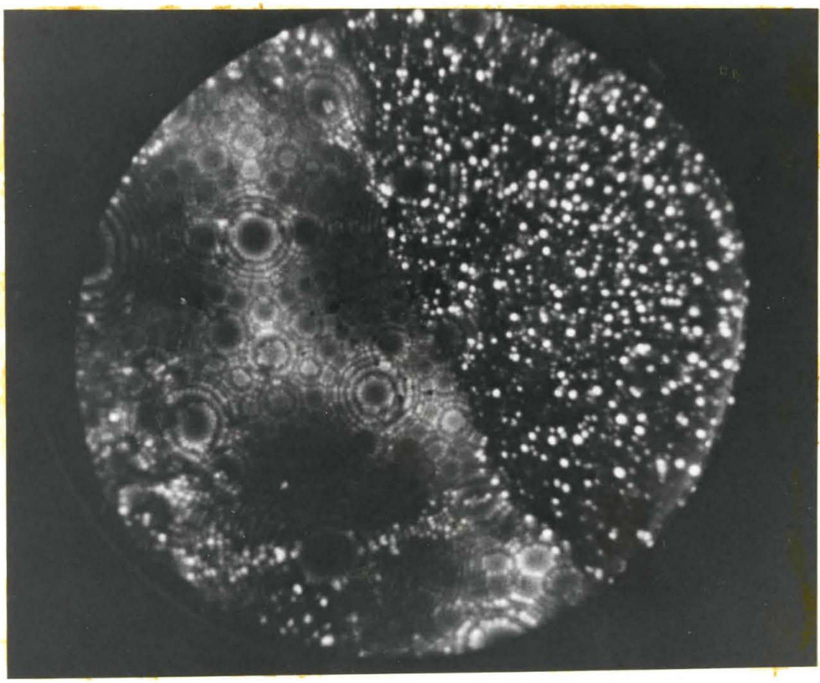

Figure 5.6 (c) The surface imaged after further field evaporation. Notice the ring structure in the deposit centered on the ledges of the $(110)_W$. BIV 13.7 KV.

observed structure is due to the amorphous nature of the deposit.

5.5 Deposition of iridium on tungsten II

In this set of experiments, a higher flux of iridium vapour (4-8 layers per minute) was used for deposition. In the experiments reported here the deposits were annealed at 1200°C for 3 hours (section 5.5.1); at 800°C for 1 1/4 hours (section 5.5.2); and at 900°C for 2 hours (section 5.5.3).

5.5.1 Deposit annealed at 1200°C for 3 hours:

The iridium vapour was deposited with the substrate temperature held at 800°C. Figure 5.7 (a) is the micrograph of the tungsten substrate before deposition. The most striking feature of the deposited and annealed surface in figure 5.7 (b) is the dark contrast of 4-fold symmetry near the {100} planes of the tungsten substrate, and the dark areas near the {111} regions. The tip has obviously become blunt (compare the BIV in figures 5.7 (a) and (b)). Figures 5.7 (c) to 5.7 (e) show successive stages in the field evaporation of the deposited surface.

The ring structure of the deposit around the central and the outlying (110) planes in figure 5.7 (c) seem to have a 6-fold symmetry and it could possibly be the (0001) plane of h.c.p. ε-phase that exists in the tungsten-iridium phase diagram(87). This structure on the central (110) disappeared on field evaporation (figure 5.7 (d)) but it persisted on the outlying {110} planes where the electric field was probably not high.

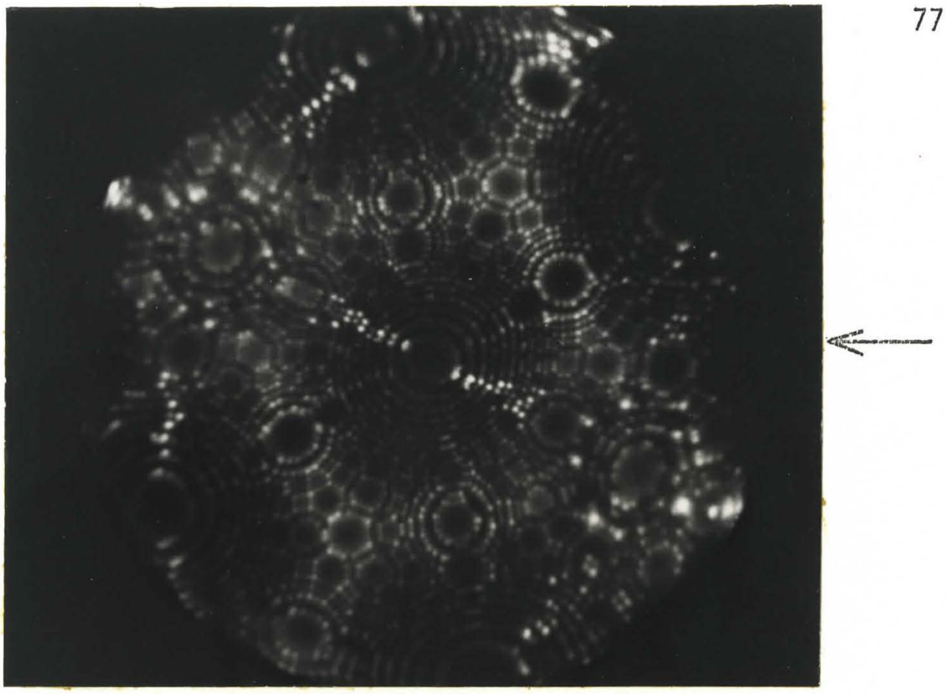

Figure 5.7 (a) Tungsten substrate. BIV 10.2 KV.

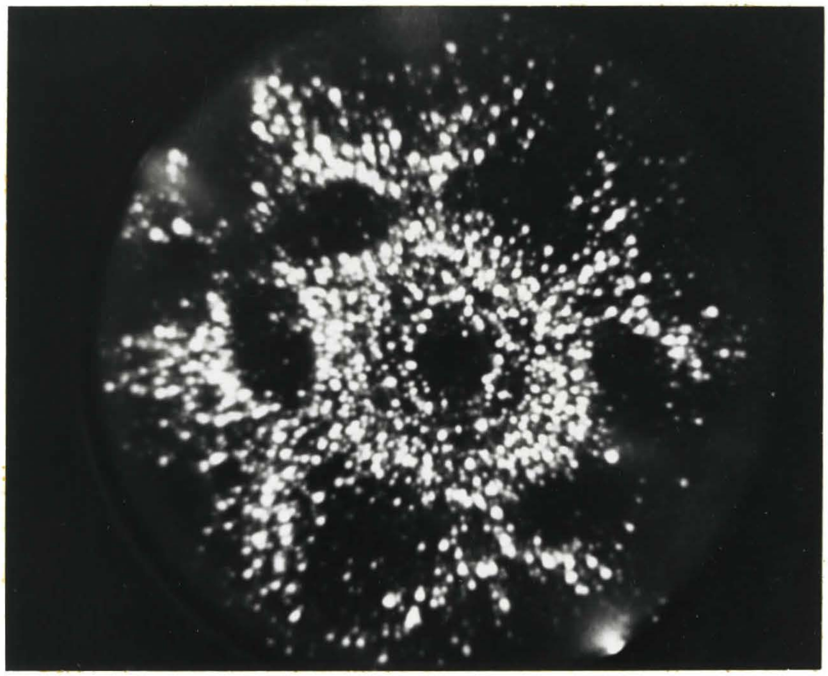

Figure 5.7 (b) The deposited surface after annealing for 3 hours at 1200°C. Note the symmetric pattern near the $\{100\}_W$ regions and the dark contrast at the $\{111\}_W$ regions. BIV 15.0 KV.

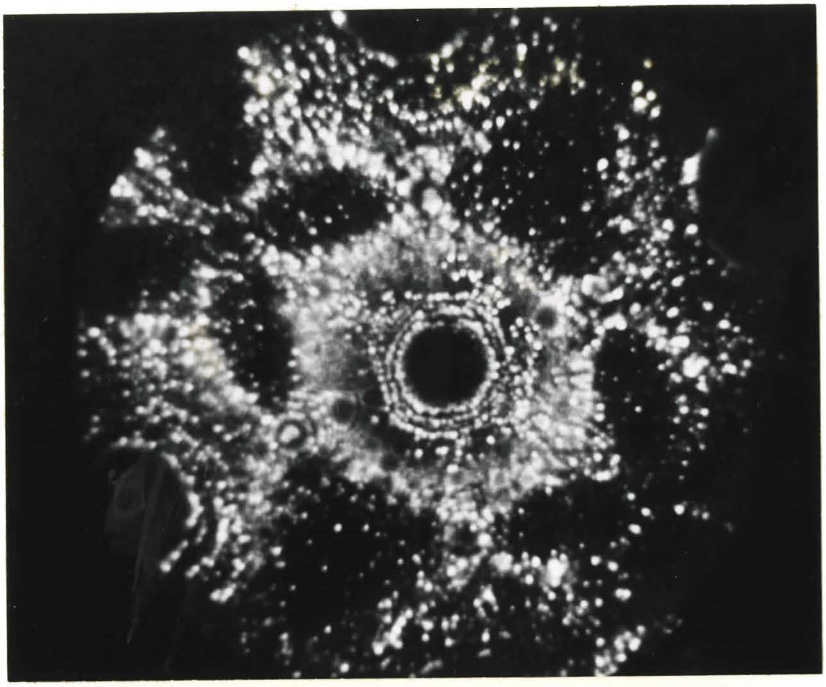

Figure 5.7 (c) Note the decoration on the edges of the $\{110\}_W$ rings.
BIV 17.9 KV.

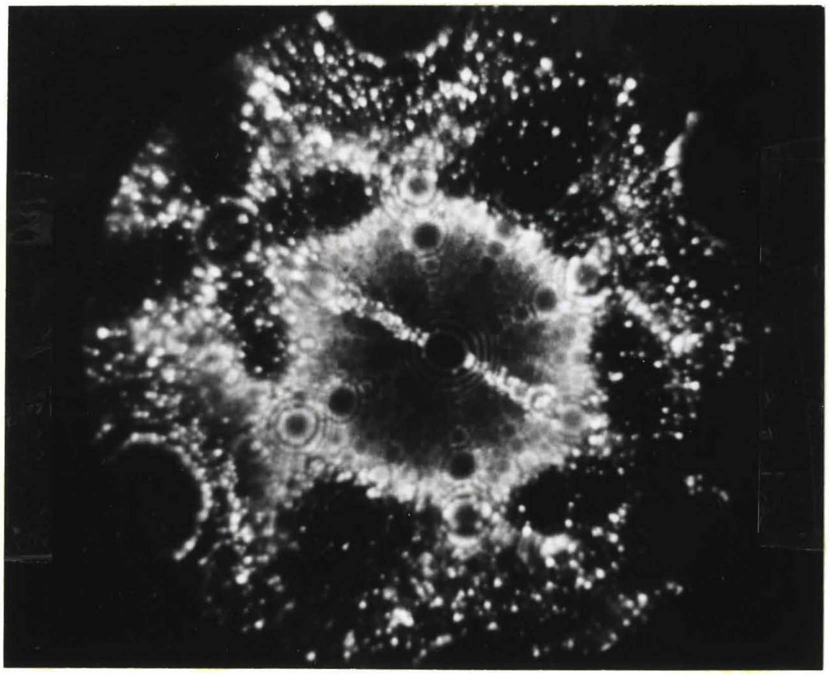

Figure 5.7 (d) There is no deposit left on the central $(110)_W$ plane.
BIV 18.0 KV.

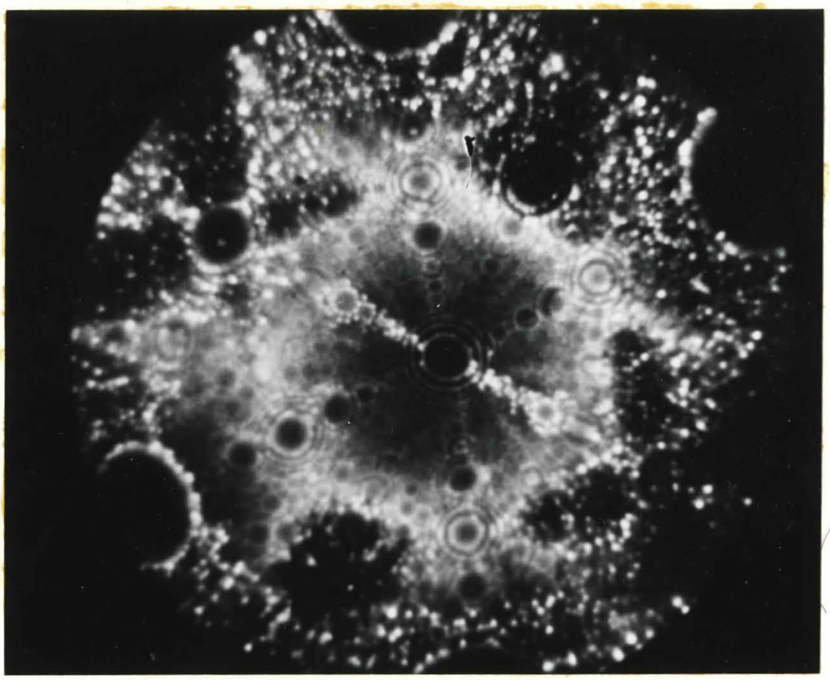

Figure 5.7 (e) The decorations on the outlying $\{110\}_W$ still persist, whereas the dark contrast in the $\{100\}_W$ and $\{111\}_W$ regions have been partially removed. BIV 18.9 KV.

The existence of the 4-fold symmetric dark band through many layers of field evaporation (as seen from the increase in BIV from 15.0 kv in figure 5.7 (b) to 18.9 kv in figure 5.7 (e)) and the retention of the same crystallographic direction throughout, shows that they run through the tungsten crystal along orthogonal {110} planes. The dark contrast observed in the {111} regions persists in a direction normal to the {111} planes. The dark contrast in these areas can be explained as follows: the material constituting the dark areas is apparently different from the tungsten substrate which exhibits well developed planes (figure 5.7 (d)). This material field evaporates at much lower fields than the adjacent tungsten substrate, probably because of being a new phase - a h.c.p. ε phase- which possibly has a lower evaporation field compared to pure tungsten.

Observation of the dark band contrast in specific crystallographic regions could be the result of preferential nucleation of the h.c.p. ε phase at the interfaces between the deposit and the {100} and the {111} regions of the tungsten surface and the movement of these interfaces in the <100> and <111> directions, respectively.

Preferred nucleation sites observed on tungsten field emitter surfaces by Jones(63) and Melmed(64) are the same as those reported here. This lends weight to the idea of preferred nucleation of the ε phase along the {100} vicinals, the {111} regions and the {110} net plane edges on the tungsten surface.

The preceding section illustrates the potential of FIM studies in examining preferred nucleation and the difficulties encountered in image interpretation when dealing with composite specimens. In the subsequent sections the resolving power of the FIM in observing the structure of two-phase interfaces in atomic detail and the difficulties involved in obtaining proper contrast at these interfaces is illustrated.

5.5.2 Deposit annealed at 800°C for 1 1/4 hours

The substrate surface before deposition is shown in figure 5.8 (a) and the initial appearance of the annealed deposit in figure 5.8 (b). The deposit presents a thermally rearranged appearance as can be seen from the presence of long chains of atoms(89). Controlled field evaporation through many layers failed to show any structure in the deposit. The image of figure 5.8 (c) was observed after the field evaporation of 60-70 layers. A prominent feature of the deposit is the presence of distinct crystallographic planes corresponding to (010), $(03\bar{1})$ and $(01\bar{1})$ planes in the substrate. Apparently, there are about three crystals in the deposit, although their boundaries are not clearly discernible. Indexing of the deposit cannot be performed with any confidence. The interface between the deposit and the substrate is not very distinct partly because of the poor quality of the micrographs. It is interesting to note that a spiral contrast is observed at the interface near the (010) plane of tungsten (figure 5.8 (c)).

The appearance of fairly well developed crystal planes in the deposit suggests that the higher rate of vapour deposition was conducive to the formation of a crystalline deposit. This could

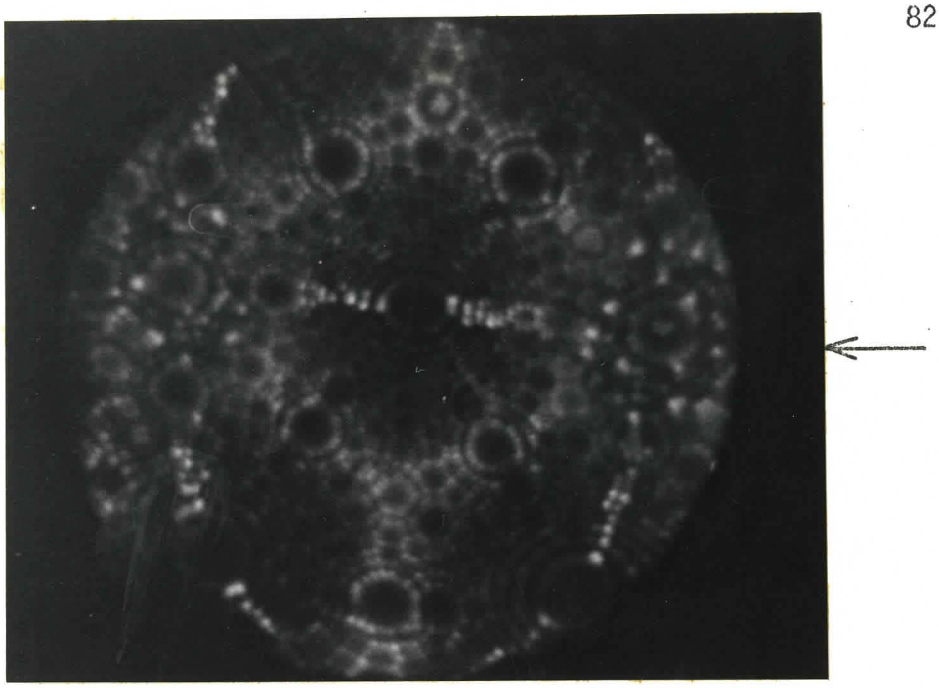

Figure 5.8 (a) Tungsten substrate. BIV 8.0 KV.

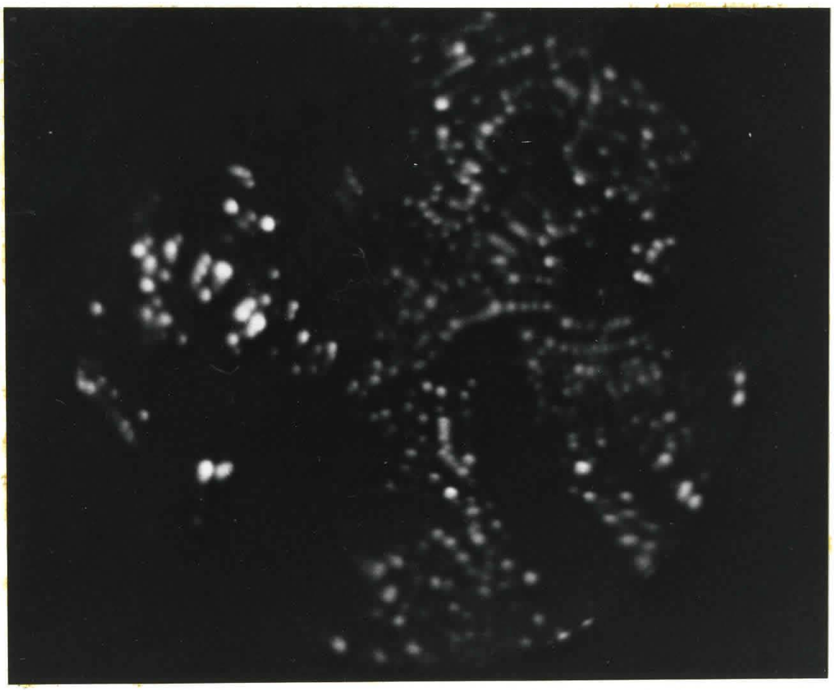

Figure 5.8 (b) Iridium deposit on tungsten after annealing. The deposit presents a thermally annealed appearance. BIV 7.3 KV.

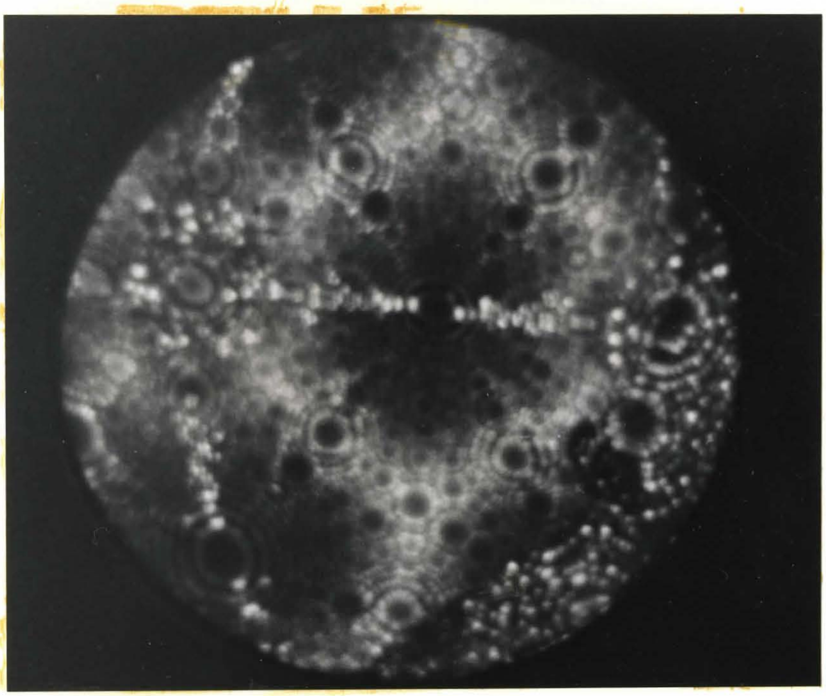

Figure 5.8 (c) Three distinct planes corresponding to (010), (03$\bar{1}$) and (01$\bar{1}$) planes of tungsten are present in the deposit. Note the spiral configuration at the interface near the $(010)_W$ plane. BIV 11.1 KV.

probably be due to the partial elimination of the effect of contamination arriving on the tip. Annealing at a higher temperature would probably induce crystallization over the entire deposit. The fact that crystallinity is observed specifically along the perifery of the micrograph suggests that crystalline overgrowth is easier on the flatter areas of the field ion emitter. In other words, the field evaporation end form of field ion emitters is perhaps not the most ideal substrate for growth of large crystals from vapour.

5.5.3 Deposit annealed at 900° for 2 hours

Figure 5.9 (a) shows the tungsten substrate before deposition and figures 5.9 (b) to 5.9 (f) show the deposited surface at different stages of field evaporation. The annealing treatment in this experiment has resulted in the crystallization of the deposit. The crystalline structure of the deposit becomes more apparent as field evaporation is continued (fig. 5.9 (e)) probably due to the formation of a more regular field evaporation surface structure. It is obvious that the deposit is polycrystalline. The two prominent deposit planes in figures 5.9 (e) and (f) are probably the {111} planes of iridium and are centered around the {123} planes of the substrate. Clear boundaries between the various crystals are not discernible and it appears that considerable defect structure is frozen into the deposit. The polycrystalline nature of the deposit could be due to the presence of a lower level of the contamination which led to the formation of a localized amorphous structure, thus stabilizing the

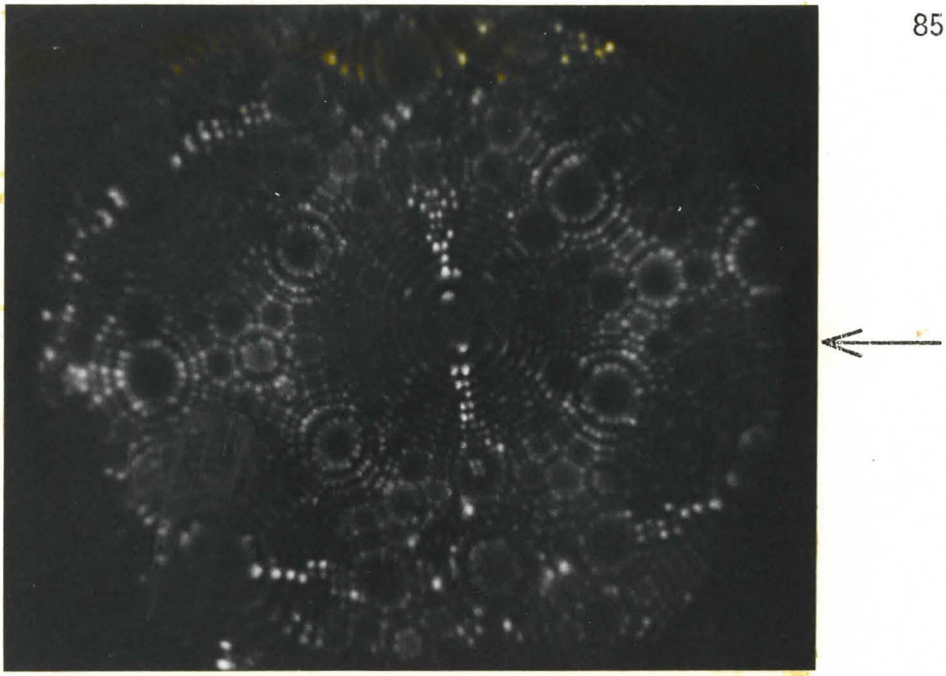

Figure 5.9 (a) Tungsten substrate. BIV 8.3 KV.

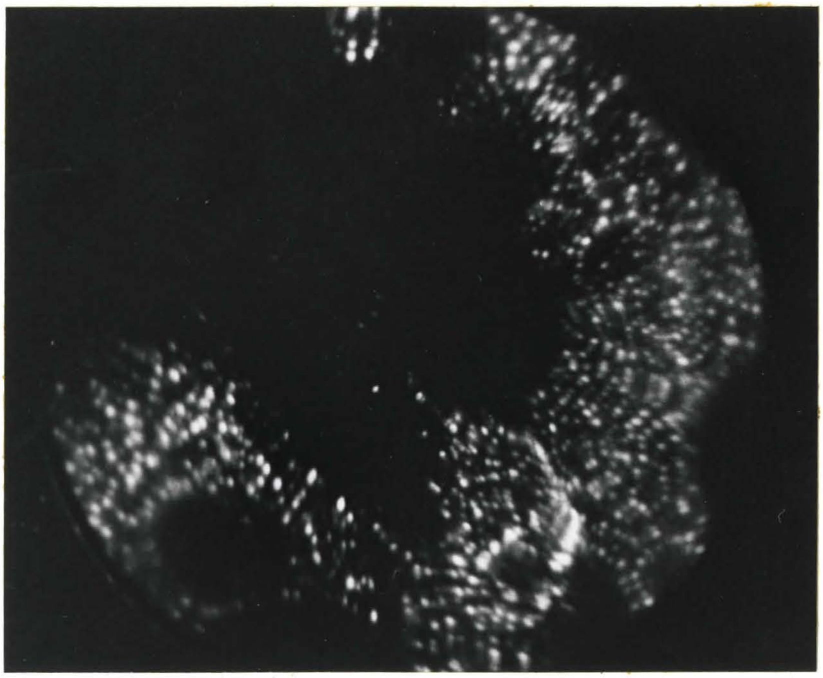

Figure 5.9 (b) The deposit after annealing at 900°C for 2 hours. The crystalline nature of the deposit is not apparent. BIV 9.0 KV.

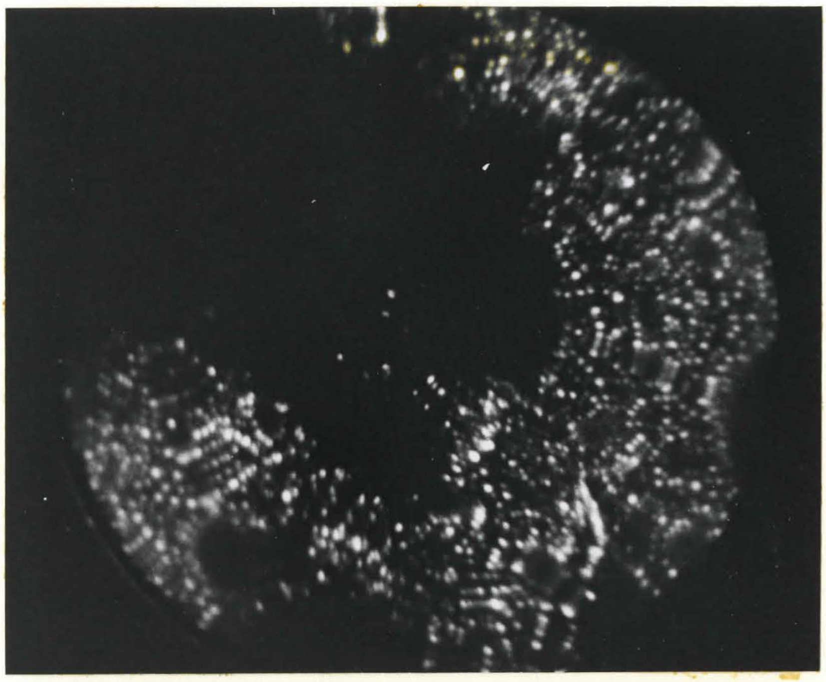

Figure 5.9 (c) The deposit after further field evaporation. BIV 9.8 KV.

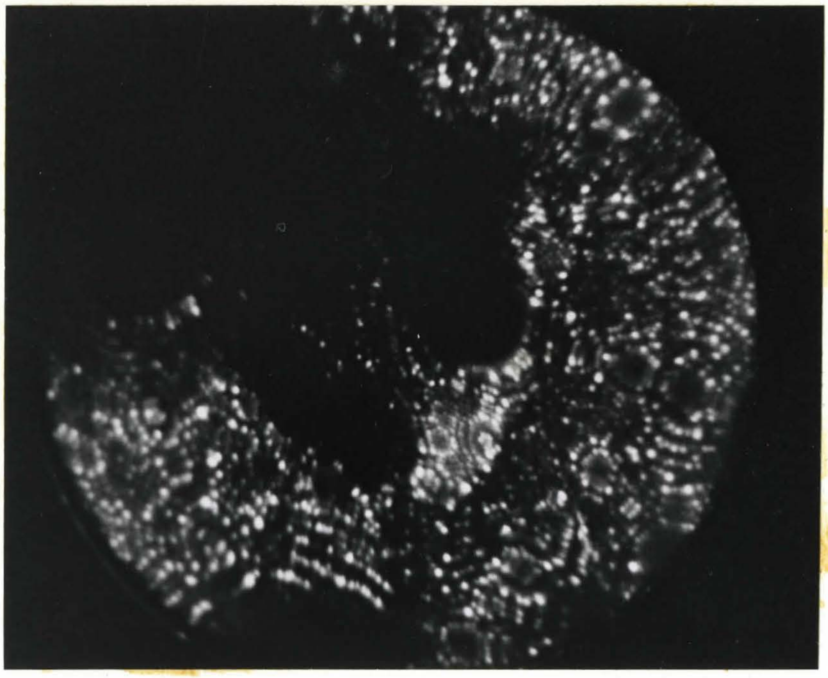

Figure 5.9 (d) The polycrystalline nature of the deposit is apparent. Some part of the substrate is visible (bright contrast). BIV 11.6 KV.

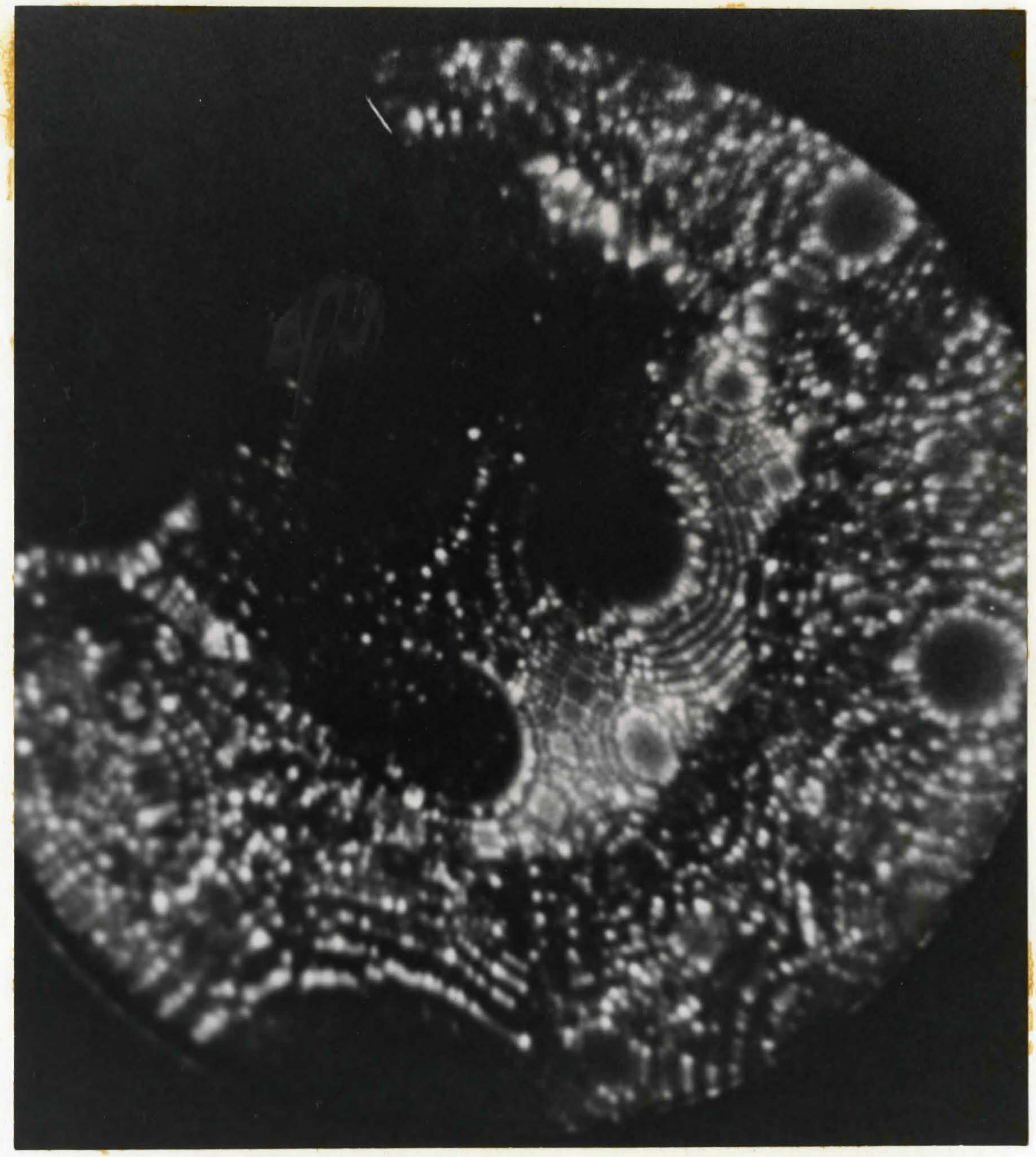

Figure 5.9 (e) Further field evaporation has led to the reappearance of more of the tungsten substrate. A very clearly defined interface is visible. BIV 12.5 KV.

Figure 5.9 (f) The interface has receded and a larger area of the substrate is visible. BIV 13.0 KV.

defect structure in the deposit.

The substrate and the deposit atoms can be easily distinguished by their relative brightness. Tungsten atoms generally appear brighter than the iridium atoms. The use of work function (see table 5.1) as the criterion for comparing the visibility of the two species (55,56) gives this result. However, caution must be exercised in attempting to identify iridium or tungsten atoms at the interface.

In figures 5.9 (e) and 5.9 (f) there is a dark band contrast (low image intensity) all along the iridium side of the interface. Such a contrast is due to a rather abrupt increase in the local radius of curvature of the iridium at the deposit/substrate interface. A similar contrast has been reported elsewhere(90). The abrupt change in radius at the interface could be due to the differences in the rates of field evaporation of the atoms on either side of the interface, due to differences in the nature of the atomic species involved.

In vapour deposition studies of the molybdenum/iridium system, Whitmell(69) has obtained epitaxial deposits of iridium on molybdenum. The interfacial contrast obtained in his experiments are unsuitable for the examination of interfaces because only the iridium atoms imaged right up to the interface, whereas the molybdenum did not image for the distance of a few hundred (100-200) angstroms from the interface. This indicates the difficulties involved in obtaining a proper contrast at two-phase interfaces. In the present experiments, two phase interfaces have been successfully imaged as can be seen from the contrast obtained at the interfaces in figures 5.9 (e) and 5.9 (f).

The completely dark contrast observed in the areas directed away from the direction of the incident vapour flux (figures 5.9 (b) to 5.9 (f)) can be explained as follows: these areas of the substrate probably have very little iridium on them and have thermally faceted during annealing. Such a faceting has presumably been prevented in other imaging areas due to the presence of thick overlying deposits. During imaging the protuberant deposit and the non-rearranged substrate tungsten show up, whereas the thermally faceted areas have too large radii for imaging and hence give a dark contrast. This dark contrast is probably compounded due to the small amounts of iridium present in these areas which have a reduced ionization probability of helium atoms over them.

There are a few interesting areas in the interface which correspond to a good fit across the interface. The area marked 1 in figure 5.9 (e) shows the continuity of ring structure across the interface, though, the deposit plane is itself not visible to a great extent. The area marked 2 in figure 5.9 (e) shows an interface where the deposit atoms do not image right at the interface (possibly due to irregular field evaporation), but an extrapolation of the ring structure in the deposit right up to the interface shows a tendency in the deposit to effect a good matching across the interface. The area marked 3 in figure 5.9 (f) shows a complete matching between an iridium chain of atoms and the rings of a tungsten (211) plane and a mutual sharing of a short length of tungsten atoms at the interface. The area marked 4 in figure 5.9 (f) shows the sharing of a chain of atoms at the interface by well developed planes in the substrate and the deposit. (In all the above cases, the relative brightness of the atoms at the interface was used as a guide for the identification of the atomic species.)

The ring matching effect observed can be interpreted as a tendency of the atoms to obtain good registry across the interface if the atoms on either side are on the same level (the areas marked 3 and 4 in figure 5.9 (f)). The ring matching effect observed in chains of atoms that are at different levels can be interpreted as a surface step formed while obtaining registry at the interface (the area marked 2 in figure 5.9 (e)).

A prominent feature of the interfaces observed is that the interfaces are composed of many small steps (a few angstroms wide) within the surface of the field emitter. Though the steps observed in this case are probably due to the geometry (curved nature) of the interface, it gives us a clue about the possibility of such steps existing two phase interfaces for the purpose of obtaining a good matching as well as low energy configuration at the interface.

However, it must be noted that the interfacial effects observed here are not entirely due to bulk matching of the phases meeting at the interface. The general tendency of the deposit to exhibit a good fit at the interface could be due to the thinness of the deposit near the interface. A thin slice of the deposit at the interface would strongly feel the lattice forces of the bulk substrate(68) as well as the bulk deposit resulting in an apparently good matching at the interface.

Though it has not been possible to observe the fine structure of two phase interfaces relating to small translations of atoms at the interface, it is hoped that obtaining large crystals of the deposit with an established orientation relation to the substrate would present a greater opportunity to utilize the potential of the field ion microscope to the fullest extent.

CHAPTER 6

CONCLUSIONS

1 A moderately high vacuum (10^{-8} torr) is sufficient for vapour deposition experiments in a FIM involving the observation of interfaces between thick deposits and the substrate.

2 From the vapour deposition experiments conducted, it is concluded that a relatively fast rate of deposition accompanied by prolonged anneal for three hours at a moderate temperature ($\underset{\sim}{\sim}$900°C) should yield epitaxial growth of iridium on tungsten.

The surface of the field ion emitter is probably not the most ideal one for the epitaxial growth of a deposit. A thermally rearranged surface similar to the surfaces of the emitters used in field electron emission microscopy would probably be better suited for epitaxial growth. The suitability of such a substrate for imaging by field ion microscopy and obtaining a satisfactory contrast at the interface has to be investigated.

3 An irregular bright and dark contrast observed in some of the deposits has been attributed to the presence of contaminant atoms incorporated into the deposit. This has been tentatively identified as being an amorphous metallic glass.

4 High temperature annealing of iridium deposits on a tungsten substrate results in specific crystallographic contrast effects. This has been tentatively identified as being due to preferred nucleation, of a h.c.p. ε phase at the deposite/substrate interface and a high mobility of the specific interfaces into the tungsten crystal.

5 Provided a proper contrast is developed at an interface being imaged, the extent of atomic matching at the interface can be clearly observed in the FIM.

Though the point resolution of the FIM is 2-3 Å at 77°K, it is possible to obtain a better resolution by comparing the positions of adjacent atoms and detect relative translations of the order of an angstrom or less.

6 Several small steps (of the order of a few angstroms) have been observed at interfaces between iridium and tungsten. The accuracy of the stereographic analysis is good to within a few degrees (±3°) in the identification of prominent boundary planes, but not in the indexing of small steps on the boundary.

SUGGESTIONS FOR FUTURE WORK

It is felt that the nature of the amorphous deposit needs to be firmly established. This can be achieved by conducting vapour deposition experiments in a UHV field ion microscope, carefully controlling the impurity level. Once the nature of the deposit had been established the resolution of the field ion microscope could be exploited in understanding the structure of amorphous phases.

Exploration of the possibility of growing vapour deposits on thermally rearranged field emitters for the observation of interfacial structure may prove to be very fruitful.

Field evaporation and field ion imaging in the presence of mixtures of image gases might resolve the existing difficulties in obtaining proper contrast at two phase interfaces.

Established crystallographic directions in field ion micrographs could probably be used in identifying directions in small steps at interfaces.

The use of image intensification systems would enable us to obtain more information out of the experiments than has been possible with the present system of photography. First, the chances of overlooking any interesting features in the image would be reduced. Secondly, the reduced exposure time for recording the images would enable closer sequences of the image to be recorded without noticeable changes in the image. Finally, the short exposure needed for recording the image would allow fine details such as very dim image spots to be recorded, which generally tend to be lost during extended exposures.

Finally, an extensive use of the atom-probe field ion microscope would probably resolve most of the uncertainties in image interpretation and promote a better understanding of the nature of materials.

References

1. Müller, E. W. Advances in electronics and electron Physics 13(1960) 83.
2. Gomer, R. Field emission and field ionization, Harvard University Press (Cambridge) 1961.
3. Brandon, D. G. Field ion microscopy, Eds. J. J. Hren and S. Ranganathan, Plenium Press, New York, (1968) p.28.
4. Southon, M. J. ibid page 6.
5. Müller, E. W. and T. T. Tsong. Field ion microscopy, principles and applications, Elsevier, New York (1969).
6. Müller, E. W. Z. Physik 106(1937) 541.
7. Müller, E. W., J. Panitz and S. B. McLane. Rev. Sci. Instr. 38(1968) 89.
8. Schottky, W. Z. Tech. Physik 14(1923) 63.
9. Müller, E. W. and K. Bahadur Physical Reviews 102(1956) 624.
10. Bohm, D. Quantum Theory, Prentice Hall, New York (1951).
11. Tsong, T. T. and E. W. Müller J. Chem. Phys. 41(1964) 3279.
12. Knor, Z. and E. W. Müller Surface Science 10(1968) 21.

13.	Moore, A. J. W. and D. G. Brandon	Phil. Mag. 18(1968) 679.
14.	Southon, M. J.	Ph.D. Thesis Cambridge University 1963.
15.	Müller, E. W.	J. Appl. Phys. 28(1957) 1.
16.	Southon, M. J. and D. G. Brandon	Phil. Mag. 8(1963) 579.
17.	Müller, E. W.	Phys. Rev. 102(1956) 618.
18.	Gomer, R. and L. W. Swanson	J. Chem. Phys. 38(1963) 1613.
19.	Brandon, D. G.	Brit. J. Appl. Phys. 14(1963) 474.
20.	Tsong, T. T.	Surface Science 10(1968) 102.
21.	Brandon, D. G.	Surface Science 3(1965) 1.
22.	Gomer, R.	J. Chem. Phys. 20(1952) 1772.
23.	Moore, A. J. W.	J. Phys. Chem. Solids. 23(1962) 907.
24.	Müller, E. W.	Quart. Rev. (Chem. Soc. Lond.) 23(1969) 177.
25.	Müller, E. W., S. B. McLane and J. A. Panitz	Surface Science 17(1969) 430.
26.	McKinney, J. T. and Brenner, S. S.	16th Field Emission Symposium, Pittsburg 1969.
27.	Müller, E. W. and J. A. Panitz	14th Field Emission Symposium, Washington D.C. 1967.
28.	Müller, E. W., J. A. Panitz and S. B. McLane	Rev. Sci. Instr. 39(1968) 83.
29.	Brenner, S. S. and J. T. McKinney	Appl. Phys. Letters 13(1968) 29.

30. Müller, E. W. Applications of FIM in Physical metallurgy and corrosion. Eds. R. F. Hoffman, E. W. Müller, and B. Ralph. Georgia Tech. (1969).

31. Gomer, R. and L. W. Swanson J. Chem. Phys. 38(1963) 1613.

32. Gadzuk, J. W. Surface Science 6(1967) 133.

33. Drechsler, M. and P. Wolf Proc. IV International Congress on electron microscopy, Berlin 1958. (Springer-Verlag, Berlin 1960) Vol. 1, p.835.

34. Müller, E. W. Surface Science 2(1964) 484.

35. Tsong, T. T. Surface Science 10(1968) 303.

36. Müller, E. W. Surface Science 8(1967) 462.

37. Ralph, B. and D. G. Brandon Phil. Mag. 8(1963) 919.

38. Bowkett, K. M., J. J. Hren and B. Ralph Third european regional conference on electron microscopy. Prague 1964. (Czech. Acd. Sci.) p.191.

39. Ranganathan, S. ibid p.265.

40. Bowkett, K. M. Ph.D. Thesis, Cambridge University, 1966.

41. Hirsh, P. B., A. Howie R. B. Nicholson, D. W. Pashley and M. J. Whelan Electron microscopy of thin crystals, Butterworths, London 1965.

42. Fortes, M. A. and B. Ralph — Phil. Mag. 18(1968) 787.

43. Ralph, B. — Ph.D. Thesis Cambridge University, 1964.

44. Bowkett, K. M. and D. A. Smith — Field ion Microscopy, North Holland Publishing 1970.

45. Morgan, R., and B. Ralph — J.I.S.I. 206(1968) 1138.

46. Ranganathan, S. — J. Appl. Phys. 37(1966) 4346.

47. Mott, N. F. — Proc. Phys. Soc. 60(1948) 391.

48. Brandon, D. G., B. Ralph, S. Ranganathan and M. S. Wald — Acta Met. 12(1964) 813.

49. Brandon, D. G. — Acta Met. 14(1966) 1479.

50. Ranganathan, S. — Ph.D. Thesis, Cambridge University 1965.

51. Löberg, B., H. Norden and D. A. Smith — Phil. Mag. 24(1971) 897.

52. Rayn, M. F., and J. Suiter — Acta Met. 14(1966) 847.

53. Fortes, M. A. and D. A. Smith — J. Appl. Phys. 41(1970) 2348.

54. Bayuzick, R. J. and R. S. Goodrich — Surface Science 23(1970) 225.

55. Southworth, H. N. and B. Ralph — Journal of Microscopy 90(1969) 167.

56. Southworth, H. N. and B. Ralph Phil. Mag. 14(1966) 383.

57. Dubroff, W. Ph.D. Thesis, Columbia University 1967.

58. Dubroff, W. and E. S. Machlin Acta Met. 16(1968) 1313.

59. Tsong, T. T. and E. W. Müller J. Appl. Phys. 38(1967) 545.

60. Tsong, T. T. and E. W. Müller. J. Appl. Phys. 38(1967) 3531.

61. Tsong, T. T. Applications of field-ion microscopy in Physical metallurgy and corrosion, Eds. R. F. Hochman, E. W. Müller and B. Ralph, Georgia Tech. Press 1969.

62. Pashley, D. W. Advances in Physics 14(1965) 327.

63. Jones, J. P. Proc. Roy. Soc. (Lond.) 284A,(1965) 469.

64. Melmed, A. J. J. Appl. Phys. 36(1965) 3585.

65. Montagu-Pollock, H. M., T. N. Rhodin and M. J. Southon Surface Science 12(1968) 1.

66. Smith, G. D. W. and T. S. Anderson Surface Science 24(1971) 459.

67. Moss, A. R. L. and B. H. Blott. Surface Science 17(1969) 240.

68. Whitmell, D. S. Surface Science 11(1968) 37.

69. Rendulic, K. D. and E. W. Müller. J. Appl. Phys. 38(1967) 550.

70. Bassett, G. A., J. W. Menter and D. W. Pashley. Structure and properties of thin films. New York, Wiley (1959), Eds. C. A. Neugebauer et. al.

71. Smith, C. S. Trans. ASM 45(1953) 533.

72. Malcolm, J. A. and G. R. Purdy. Trans. AIME 29(1967) 1391.

73. Aaronson, H. I., C. Laird and K. R. Kinsman. Phase transformations, ASM seminar 1968.p.313.

74. Zener, C. J. Appl. Phys. 20(1949) 950.

75. Aaron, H. B. and H. I. Aaronson. Acta Met. 16(1968) 789.

76. Hillert, M. 'The mechanism of phase transformations in crystalline solids', Institute of Metals, London, 1969, p.231.

77. Frank, F. C. and van der Merwe, J. H. Proc. Roy. Soc. Lond. 198A(1949) 205.

78. Frank, F. C. and van der Merwe, J. H. ibid p.216.

79. van der Merwe, J. H. Proc. Phys. Soc. 63A(1950) 616.

80. Brooks, H. "Metals interfaces" ASM 1952 p.20.

81. Paxton. J. Chem. Phys. 26(1957) 1769.

82. Aaronson, H. I. Decomposition of austenite by diffusional processes. Eds. H. I. Aaronson and V. F. Zackay. Interscience, NY 1962 p.387.

83. Flewitt, P. E. J. Private communication

84. Hall, M. G., H. I Aaronson and K. R. Kinsman Private communication

85. Howell, P. R., T. F. Page and B. Ralph Phil. Mag. 25(1972) 879.

86. Hansen, M. Constitution of binary alloys. McGraw Hill, 1958.

87. Shunk, F. A. Constitution of binary alloys. Second Supplement, McGraw Hill, 1964.

88. Turnbull, D. Contemp. Phys. 10(1969) 473.

89. Bassett, D. W. Proc. Roy. Soc.(Lond) A256(1965) 191.

90. Davies, D. M. Ph.D. Thesis, Cambridge University 1970.